Scientific Report

of the Group of G. Weigelt

1999 — 2002

Young stellar objects, evolved stars, active galactic nuclei, long-baseline infrared interferometry, and theoretical studies

1 Young Stellar Objects

Young stellar objects (YSOs) are typically embedded in remnant material from their formation. This material is often being accreted onto the central object, and this process in turn can lead to spectacular outflows and jets, which arise near the heart of the system and then interact with more distant material. Near-infrared bispectrum speckle interferometry delivers high spatial resolution in a wavelength range where interesting structures often dominate the emission, giving new insights into the distribution and physical properties of dusty circumstellar matter and the behavior of outflows close to their launching sites. One of the main topics of our current work is, therefore, the study of infrared counterparts of bipolar radio CO outflow sources (e.g., S140, R Mon, Mon R2, K 3-50, and AFGL 2591).

1.1 Bispectrum Speckle Interferometry of the Massive Protostellar Object S140 IRS 1: Discovery of Multiple Outflows

Figure 1 shows bispectrum speckle interferometric observations of the deeply embedded massive YSO S140 IRS 1. A K'-band (2.15 μm) diffraction-limited resolution of 76 mas ($\sim$ 70 AU) is achieved with the SAO 6 m telescope, as well as a dynamic range of more than 8 magnitudes and a field of view of $13'' \times 21''$. Our image exhibits many previously unseen complex structures. In addition to the bright, elongated, and very clumpy outflow cavity (yellow) pointing from the central source to the south-east, we find several arc-like structures north-east of IRS 1, extended diffuse emission south of IRS 1, and several new point sources. The complex of the three north-eastern arcs shows a systematic positional offset of their bow-shaped tips; this structure could be well explained as the successive sites of impact of a precessing jet-driven outflow. Our seeing-limited images of the S140 region in the light of the 2.12 μm molecular hydrogen emission line (a convenient tracer of shocked gas) show strong H_2 shock emission at the location of the north-eastern arc system as well as to the south-west of IRS1, clearly demonstrating the presence of outflow activity in the north-east/south-west direction. These results provide direct evidence of the existence of two distinct bipolar outflow systems originating simultaneously from IRS 1, the previously known 160°/340° outflow found in CO radio observations, and a previously unknown flow in the 20°/200° direction revealed by our speckle and H_2 observations. This can be understood if one assumes that S140 IRS 1 is a close binary system in which each star is responsible for one of the outflows. The precession of the outflow that created the three cavities in the north-western lobe can be explained as the consequence of a misalignment between the disks and the orbital plane of the system, which

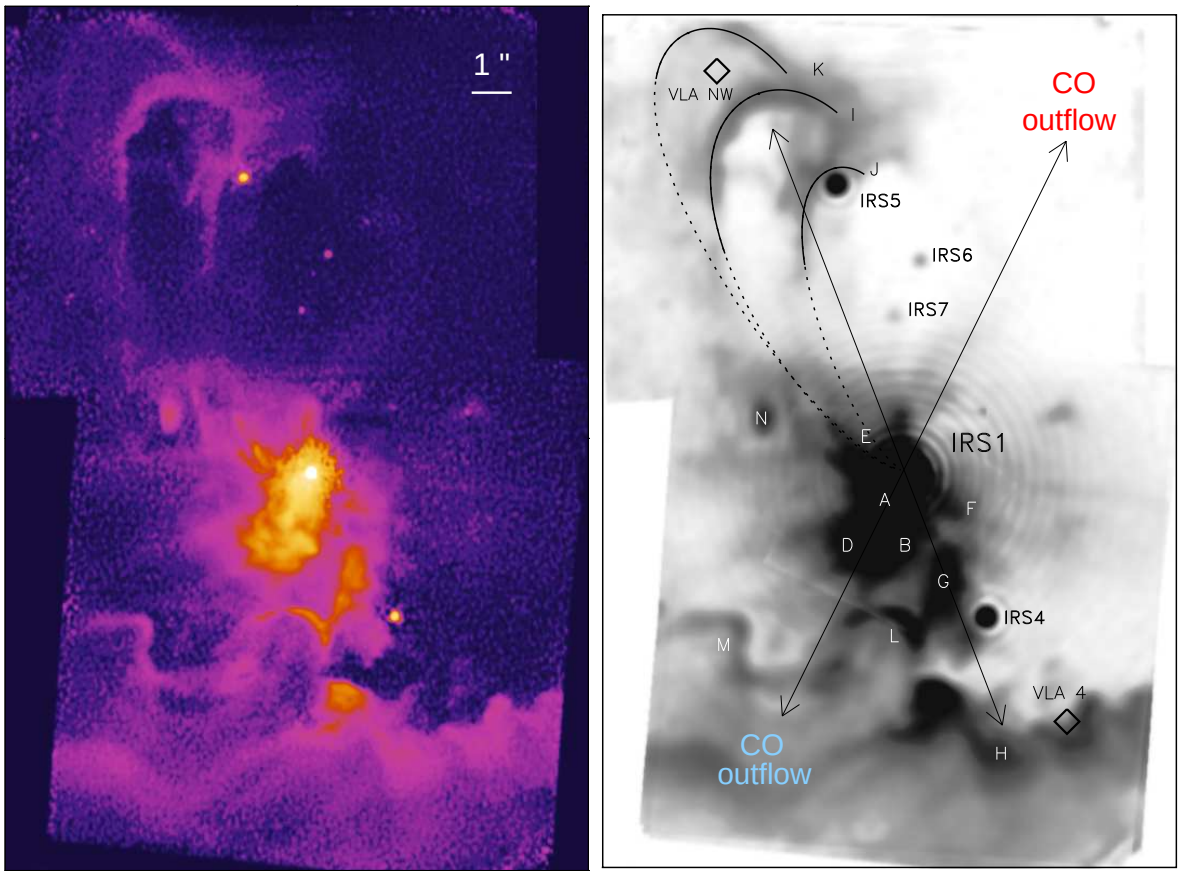

Figure 1: Bispectrum speckle interferometry of S140 IRS 1. *Left:* Pseudocolor representation of our K'-band mosaic image of a $13'' \times 21''$ area with a diffraction-limited resolution of 76 mas. *Right:* Grayscale representation of the same image reconstructed with a reduced resolution of 240 mas. The curved lines show the shapes of the theoretical cavity models which were compared with the observations. The arrows indicate the four major outflow directions.

causes precession of the non-coplanar disk. Our results clearly demonstrate that S140 IRS 1 has a very complex environment and deserves further observational efforts. In particular, proper motion measurements of the near environment will answer many of the dynamical questions.

1.2 Detection of a Precessing Jet from the YSO S140 IRS 3

S140 IRS 3 is an intermediate-mass YSO located $\sim 8''$ east of IRS 1. We reconstructed a bispectrum speckle interferometric K-band image with a resolution of 150 mas and a seeing-limited H_2 line image. Our speckle image (Fig. 2) resolves IRS 3 into three point sources: a close binary with separation $0.63''$ and a third component $1.3''$ away, and an extended diffuse feature north-east of IRS 3 (S-shaped structure). This feature is the innermost part of an extended structure, at least $15''$ long, which is pointing towards a bow-shock located $90''$ away from IRS 3. We find strong H_2 line emission associated with this feature, suggesting the presence of shocks caused by the collision of outflowing material with the ambient medium. The S-shaped structure of this feature can be well reproduced by a model assuming a precessing outflow from IRS 3. Furthermore, we find several elongated features pointing away from

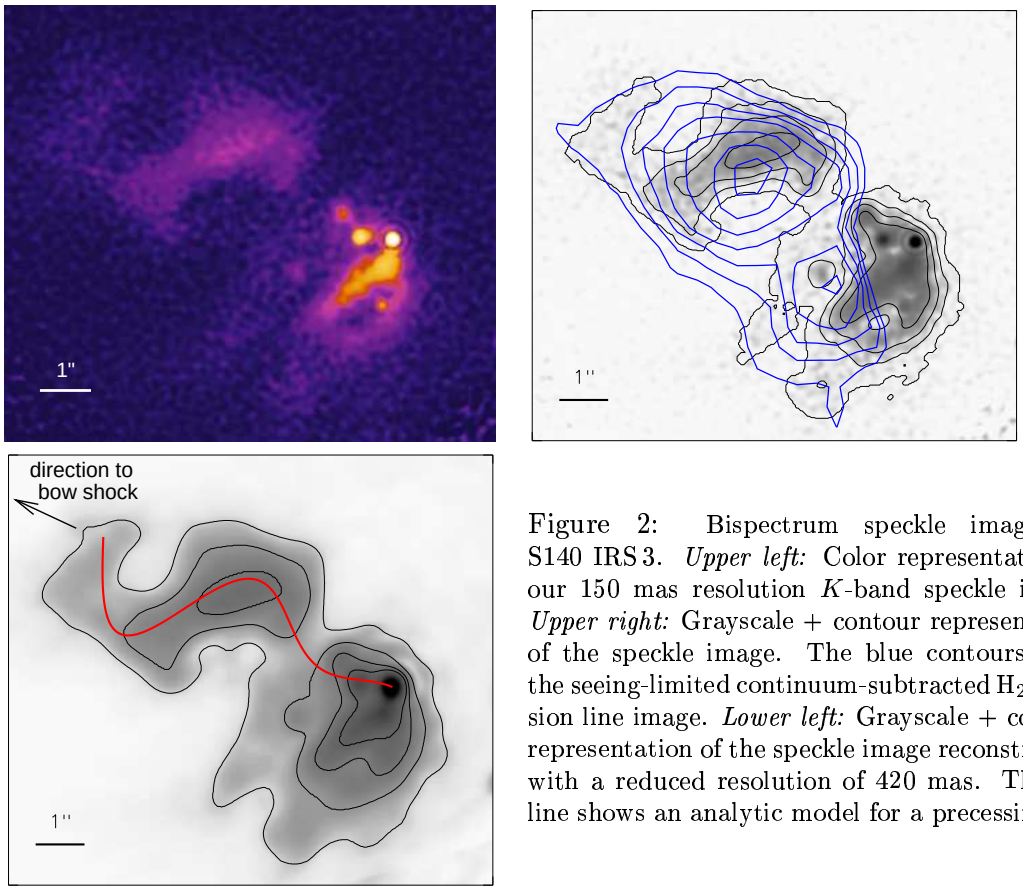

Figure 2: Bispectrum speckle images of S140 IRS 3. *Upper left:* Color representation of our 150 mas resolution K-band speckle image. *Upper right:* Grayscale + contour representation of the speckle image. The blue contours show the seeing-limited continuum-subtracted H_2 emission line image. *Lower left:* Grayscale + contour representation of the speckle image reconstructed with a reduced resolution of 420 mas. The red line shows an analytic model for a precessing jet.

IRS 3 in a southward direction. Some of these features also exhibit strong H_2 line emission, suggesting that IRS 3 drives outflows in several directions.

1.3 Bispectrum Speckle Interferometry of the Herbig Be Star R Mon: First Resolution of the Inner Dust Environment

In our near-infrared speckle images of the intermediate-mass YSO R Mon (Fig. 3) with unprecedented diffraction-limited resolution of 55 mas ($\sim$ 44 AU; H band) and 76 mas ($\sim$ 61 AU; K band), the binary companion R Mon B appears as an unresolved point source, but the primary R Mon A is elongated in the K band and significantly extended in the H band. The most prominent new feature is a bright arc-shaped structure, pointing away from R Mon A to the north-west. We interpret this feature as the surface of a dense structure near the thick circumstellar disk or torus around R Mon. Our images also reveal several twisted filaments of helical shape which are similar to the twisted filaments in the outer parts of the nebula. The region along the polar axis of the star/disk system and inside the narrow parabola through the arc-shaped speckle feature seems to be essentially free of diffuse material; probably, the fast jet from R Mon A (P.A. 350°) has cleared a narrow path (outflow cavity) along the jet axis, which is therefore now empty. The diffuse filamentary structures above the disk plane might trace material aligned along magnetic field lines.

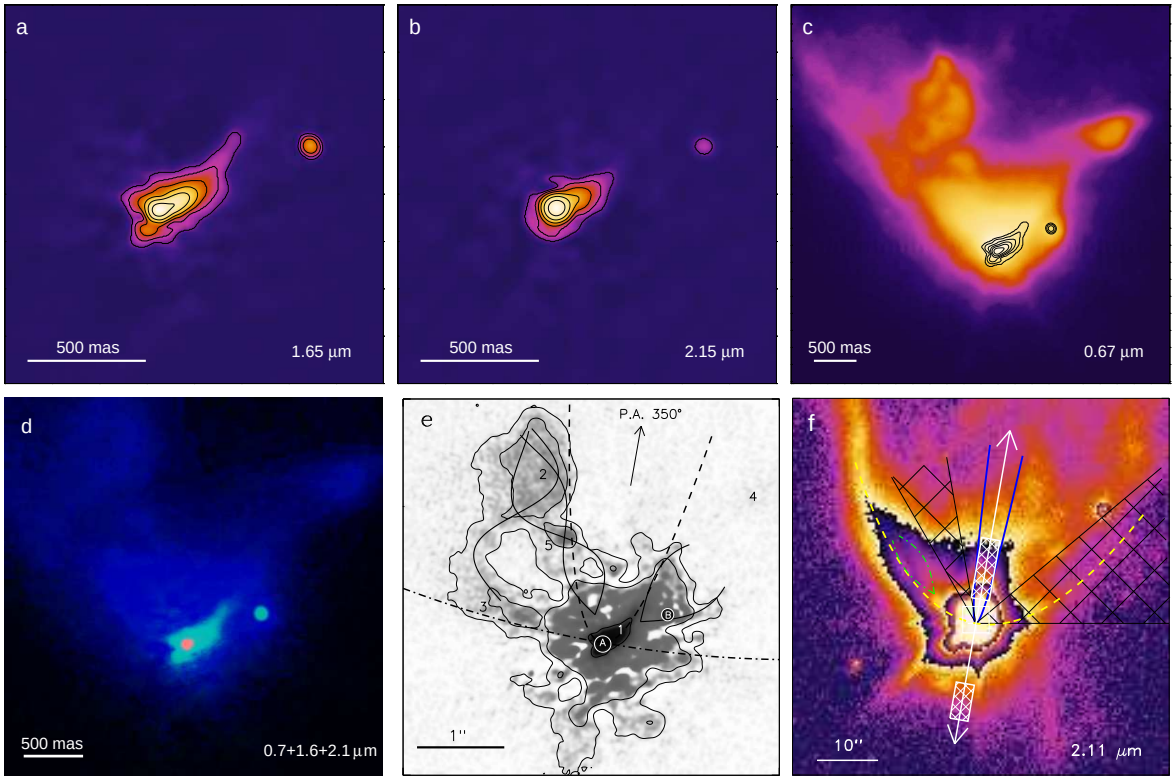

Figure 3: a,b: Central parts of our H- and K-band speckle images of R Mon. c: Archival HST/PC R-band image with contours of the H-band speckle image. d: True-color composit of the R-band (blue) HST/PC image and the H- (green) and K-band (red) speckle images. e: Grayscale + contour representation of our H-band speckle image with annotations. The dashed line is the inner parabola through the arc-shaped speckle structure. The dashed-dotted line shows the parabola defined by the large-scale fan-shaped structure of the nebulosity (yellow line in Fig. 3f). The solid sine-curves mark the helical features. f: Calar Alto K'-band image (wrapped intensity scale) of R Mon.

1.4 High-Resolution Study of YSOs in the Mon R2 Star Forming Region

Our diffraction-limited H- and K-band images of the object IRS 3 in the Mon R2 star forming region show a close triple system surrounded by strong diffuse nebulosity and several additional infrared sources within $3''$ of the brightest object, IRS 3 A. IRS 3 A is surrounded by a bipolar nebula, suggesting it is embedded in a thick circumstellar disk or a torus with polar cavities. The nebula appears in blue color in our $H+K$ composite image since it is dominated by scattered light. IRS 3 B shows a remarkable jet-like emission feature pointing towards the north-east. This feature consists of at least three individual knots with projected separations of 110, 190, and 240 AU from IRS 3 B, which are much brighter in the K band than in the H band; its general morphology is very similar to micro-jets from other YSOs. This strongly suggests outflow activity from IRS 3 B. The orientation of the suspected micro-jet (PA 50°) is roughly perpendicular to the direction of the large-scale molecular outflow, which has a position angle of 135°/315°. The micro-jet seems, therefore, not to be related to the large-scale outflow, but it might well be related to the compact high-velocity gas associated with IRS 3. We also analyzed *Chandra* X-ray archive data and found IRS 3 A and C to be sources of hard ($3-10$ keV) and variable X-ray emission, suggesting plasma temperatures of at least 50×10^6 K. The similarity of the X-ray properties to those of Class I protostars suggests that magnetic interaction between the protostars and their circumstellar disks is the origin of the

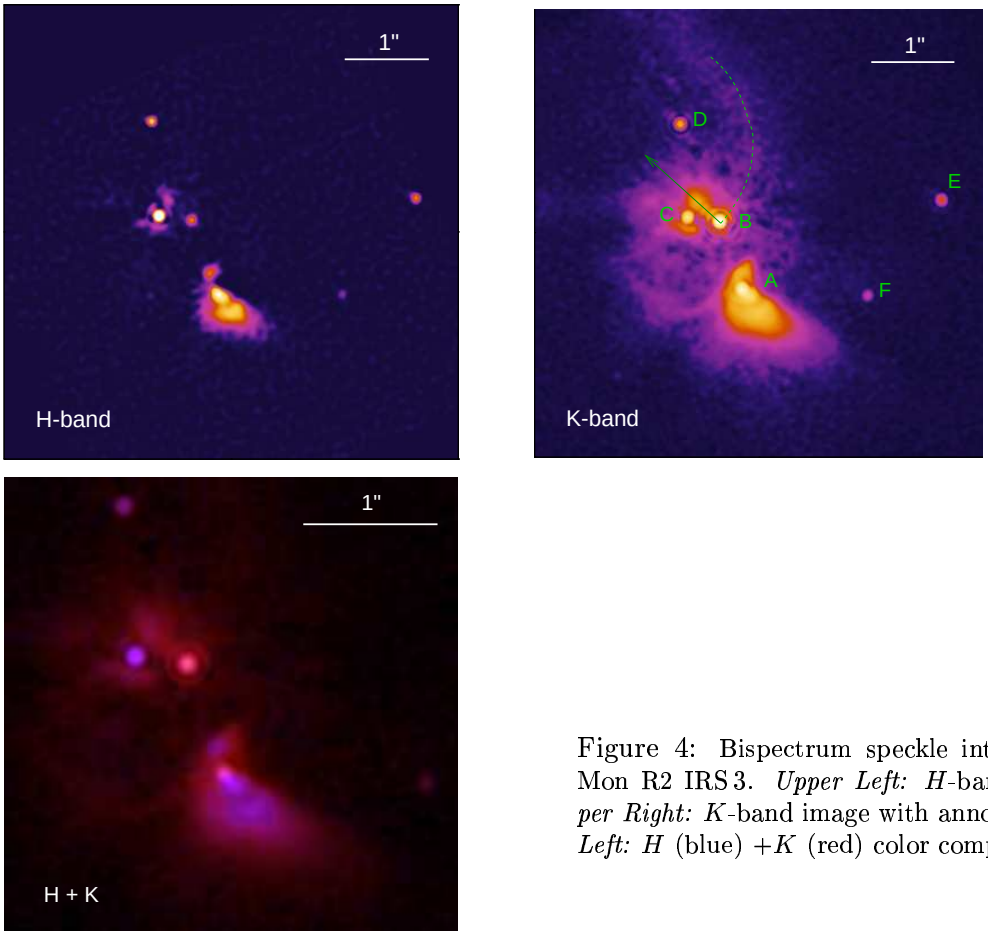

Figure 4: Bispectrum speckle interferometry of Mon R2 IRS 3. *Upper Left:* H-band image. *Upper Right:* K-band image with annotations. *Lower Left:* H (blue) $+K$ (red) color composite image.

X-ray emission; this provides indirect evidence of the presence of circumstellar disks in the intermediate- to high-mass YSOs IRS 3 A and C.

1.5 Detection of Orbital Motion in the Multiple Stars in the Orion Trapezium

Our bispectrum speckle interferometry of the Orion Trapezium stars θ^1Ori A, θ^1Ori B, and θ^1Ori C with the SAO 6 m telescope spans a period of almost six years (epochs 1995 – 2001). The diffraction-limited images (Fig. 5) with a resolution λ/D of 42 mas (J band), 57 mas (H band), and 76 mas (K band) allowed the detection of orbital motion in the systems θ^1Ori A1–2 (mean separation $\rho \sim 220$ mas, change in position angle ΔP.A. $\sim 6°$), θ^1Ori B2–3 ($\rho \sim 205$ mas, ΔP.A. $\sim 8°$), and θ^1Ori C1–2 ($\rho \sim 37$ mas, ΔP.A. $\sim 18°$). θ^1Ori C is the brightest star in the Trapezium and is responsible for the proplyds; its companion θ^1Ori C2 was discovered in 1999 with the SAO 6 m telescope. From the J, H, and K magnitudes of the system components we estimate the stellar masses of the companions in the HR diagram, finding values between $\sim 3\,M_\odot$ and $\sim 6\,M_\odot$. The companions θ^1Ori C2 and θ^1Ori B2 show clear evidence of near-infrared excess in the color-color diagram. The companions θ^1Ori A2 and θ^1Ori B3 show much stronger extinction than their primary stars. This is evidence of the presence of circumstellar material around the companions, which is quite surprising, considering the strong UV radiation and winds from the massive stars.

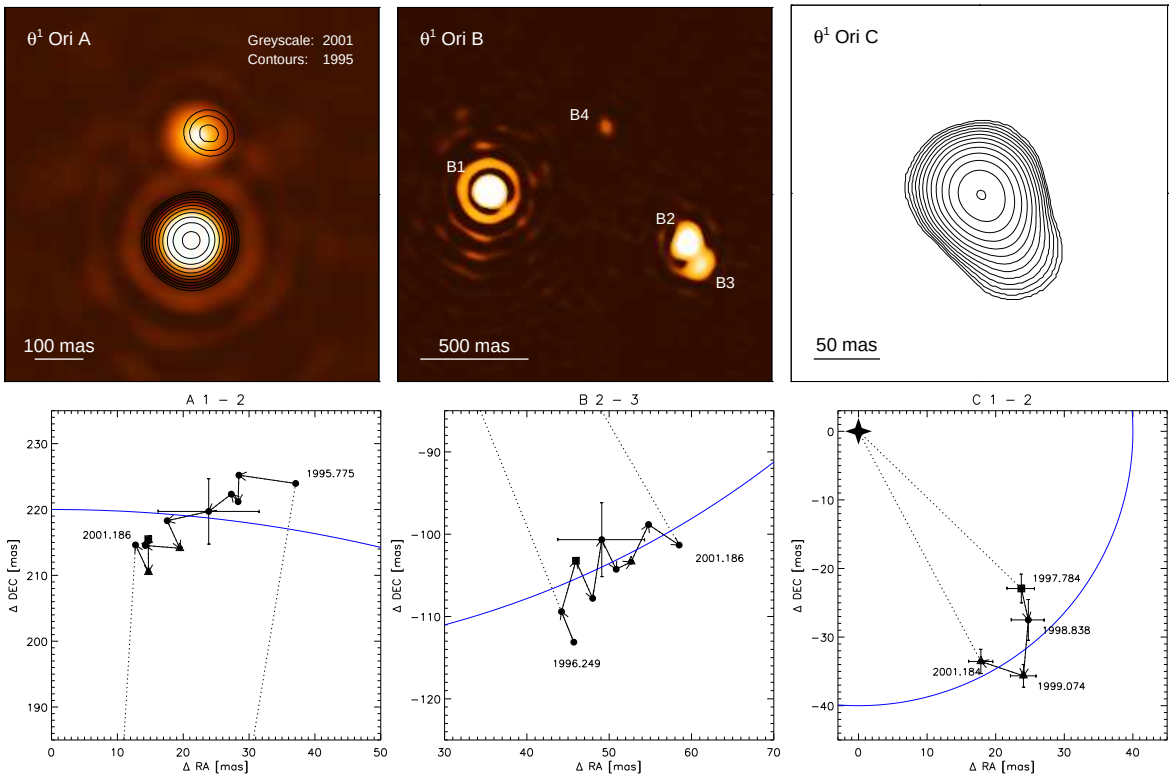

Figure 5: *Upper row:* Bispectrum speckle K-band images of θ^1Ori A (left). The heat image was reconstructed from the 2001 data, the contour image from the 1995 data. The orbital motion of the companion can be clearly seen. Bispectrum speckle K-band image of θ^1Ori B (middle; 2001 data). The faint fourth component is seen near the center of the upper half of the image. Contour representation of our J-band bispectrum speckle image of θ^1Ori C (right; 2001 data).
Lower row: orbital motion for the systems θ^1Ori A 1–2, θ^1Ori B 2–3, and θ^1Ori C 1–2. The brighter component is always placed at the origin (0,0) of the plot, the solid dots with error bars represent the observed positions of the companion. In each plot the first and last positional measurement in the data series is connected to the origin by a thin dotted line. The blue line shows a part of a circle around the primary position.

1.6 *Chandra* X-Ray Imaging Study of the Young Stellar Cluster IC 348

We have obtained a deep (53 ksec) X-ray image of the young stellar cluster IC 348 with the ACIS camera on board the *Chandra X-Ray Observatory*. Our image (Fig. 6) shows 215 X-ray sources, most of which can be identified with known cluster members. About 80% of all known cluster members with masses between $\sim 0.15\,M_\odot$ and $2\,M_\odot$ are detected in X-rays. Interestingly, we discover X-ray emission at levels of $\sim 10^{28}$ erg/sec from 7 out of 25 brown dwarfs and brown dwarf candidates in IC 348. The X-ray luminosities of the young low-mass stars are strongly correlated with the stellar bolometric luminosities and the stellar masses. For the weak-line T Tauri stars we find a tight correlation between X-ray activity and chromospheric activity, supporting the hypothesis that the chromosphere is heated by X-rays from the overlying corona. The observed X-ray properties of the brown dwarfs (and brown dwarf candidates) are very similar to those of late-type stars; we explain this behavior as the consequence of the fact that very young substellar objects are still warm enough to maintain partially ionized atmospheres which are capable of sustaining electrical currents, while in the cooler neutral atmospheres of L and T dwarfs such currents are shut off, hence no X-ray emission.

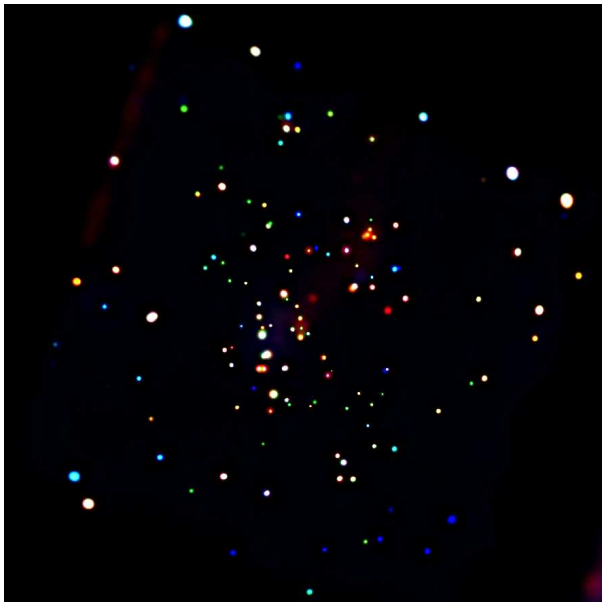

Figure 6: True-color *Chandra*/ACIS X-ray image of the young stellar cluster IC 348 (red: 0.2–1 keV, green: 1–2 keV, blue: 2–8 keV). The field of view is $17' \times 17'$.

1.7 The Full Stellar Population and Star Formation History of the Upper Scorpius OB Association

We have performed a detailed study of the stellar population in the Upper Scorpius OB association, the most nearby region of recent massive star formation. In a large multi-object spectroscopic survey we obtained spectra of 1238 stars and identified low-mass pre-main sequence (PMS) stars by their strong lithium absorption lines. Our sample contains 250 PMS stars in the mass range $\sim 0.1 - 2\,M_{\odot}$. We also studied the population of 114 intermediate/high-mass ($> 2\,M_{\odot}$) members identified in detailed Hipparcos studies. The HR diagram for the combined sample of 364 members shows that the whole stellar population is very well characterized by a narrow age distribution around 5 Myr. This confirms earlier indications that the star formation process in Upper Scorpius was triggered by a supernova shock wave originating from the nearby Upper Centaurus Lupus association. When this shock wave crossed the Upper Scorpius molecular cloud 5 Myr ago, it initiated a short but vigorous burst of star formation activity. The new-born massive stars immediately started to disperse the cloud by their ionizing radiation and their strong winds, and thereby terminated the star formation process within about 1 Myr. We also estimated individual masses for all members, and constructed an empirical mass function covering the full mass range from $0.1\,M_{\odot}$ to $20\,M_{\odot}$. We found that the initial mass function of Upper Scorpius is consistent with recent determinations of the field initial mass function. This result supports the idea that most stars in our galaxy are born in OB associations.

People involved: Th. Preibisch, K.-H. Hofmann, D. Schertl, K. Smith, G. Weigelt

Collaborations: I. I. Balega, Y. Y. Balega (Special Astrophysical Observatory, Russia), A.G.A. Brown (Sterrewacht Leiden), G.H. Herbig (Univ. of Hawaii), M.D. Smith (Armagh Observatory), H.Zinnecker (Astrophysikalisches Institut Potsdam)

2 Late Stages of Stellar Evolution: AGB Stars, Post-AGB Objects, and Massive Supergiants

2.1 The Red Rectangle: Bispectrum Speckle Interferometry with the Keck 10 m Telescope and Detailed Two-Dimensional Radiative Transfer Modeling

Observations and modeling of the envelopes of evolved stars can be used to unveil the mass-loss history, derive physical parameters, and improve our understanding of the evolution of the stars and the chemical evolution of our Galaxy. The Red Rectangle is a spectacular bipolar reflection nebula around the evolved close binary HD 44179. Although the object has been extensively studied for more than two decades, there is no full understanding of the formation and evolution of the central close binary system and its complex dusty environment. We reconstructed near-infrared images of the Red Rectangle from speckle observations at the Keck 10 m telescope, using our bispectrum speckle interferometry method. The unprecedented diffraction-limited resolution of the images (44–68 mas, Fig. 7) is 4 times higher than that of the Hubble Space Telescope.

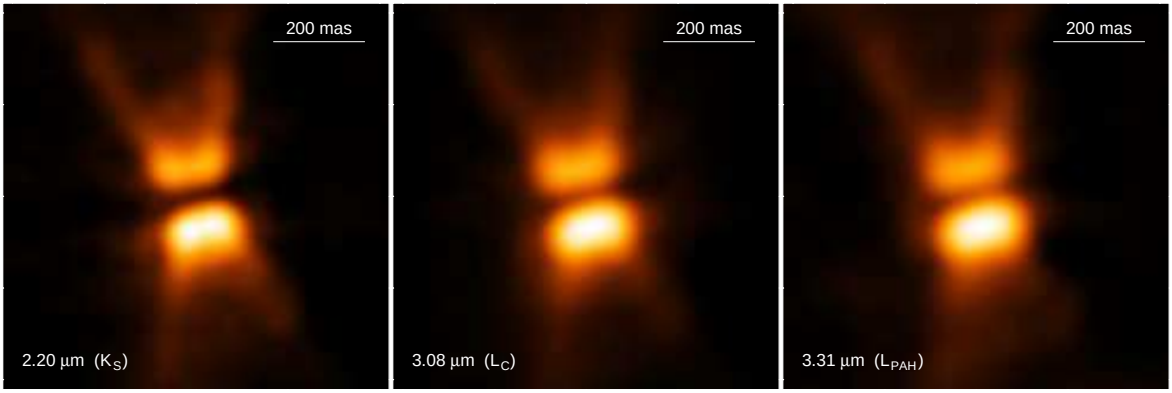

Figure 7: Diffraction-limited images of the Red Rectangle in the near-infrared K_S, L_c, and L_{PAH} filters (47, 64, and 68 mas resolution) reconstructed by the bispectrum speckle interferometry method.

The striking, biconical appearance of the Red Rectangle is preserved on scales spanning almost 3 orders of magnitude (~ 100 mas to $60''$) and from the visible light to at least mid-IR wavelengths ($\sim 10\,\mu$m), implying that very large dust grains dominate scattering. The new images supplement our previous 76 mas resolution images at 0.6–2.2 μm, allowing a more detailed interpretation. Our two-dimensional radiative transfer modeling shows that, despite the narrowness of the dark lane, the circumstellar material is distributed in a geometrically very thick toroidal envelope with bipolar conical cavities and a strong concentration of circumstellar matter toward the central close binary. The extent of the bright lobes indicates that the dense torus has a radius of ~ 100 AU.

Although our previous modeling described reasonably well large numbers of observational constraints, the new Keck images at 3.1–3.3 μm allowed us to develop a considerably improved model. The new extensive modeling, together with estimates of the interstellar extinction in the direction of the Red Rectangle, enabled us to derive its distance of 700 pc, which is twice as far as the previous, widely used but inaccurate estimate of 330 pc. Quantitatively explaining all relevant manifestations of the object, the model predicts a detailed picture (Fig. 8). The central binary is surrounded by a compact and dense, self-gravitating dusty torus with a

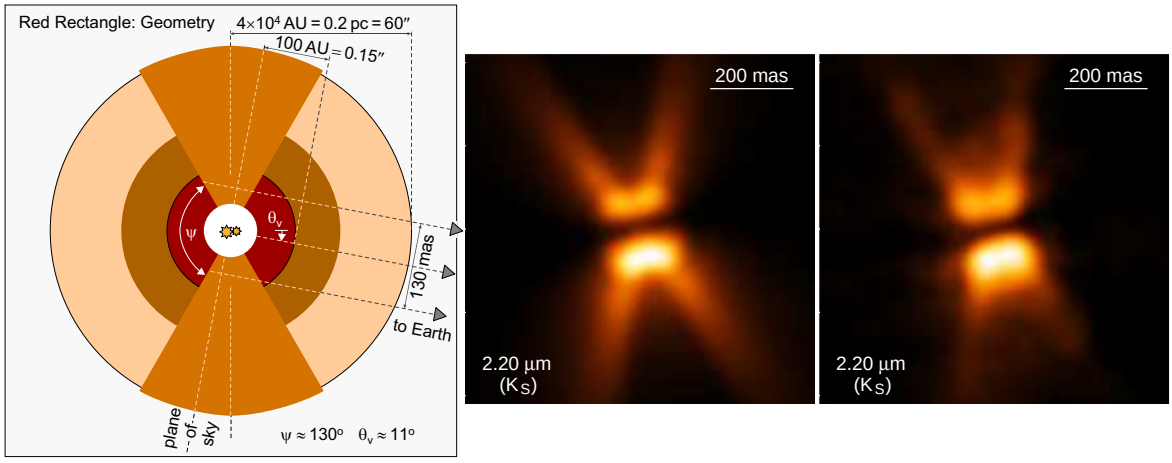

Figure 8: *Left:* Model geometry of the circumbinary environment. *Middle, right*: Comparison of our model image of the Red Rectangle (*middle*) with the observed 47 mas resolution K_S-band image.

mass of 1.2 $M_\odot$. Most of the dust mass in the dense torus is in very large particles, and, on scales of more than one arcsecond, the polar outflow regions are denser than the surrounding medium. The bright component of the spectroscopic binary HD 44179 is a post-AGB star with a mass of 0.57 $M_\odot$, a luminosity of 6000 $L_\odot$, and an effective temperature of 7800 K. We identified the invisible component as a helium white dwarf with a mass of 0.35 $M_\odot$ and a temperature of 6×10^4 K. The hot white dwarf ionizes the bipolar outflow cavities inside the dense torus, producing a small H II region observed at radio wavelengths. Our evolutionary scenario for the Red Rectangle suggests that initially ($\sim$ 1.6 Gyr ago) the binary had 2.3 and 1.9 $M_\odot$ components at a separation of $\sim 130\,R_\odot$. The spectacular nebula was formed by the ejection of a common envelope after Roche lobe overflow by the present post-AGB star.

2.2 NML Cyg: A Luminous Supergiant with Multiple Shell Structures

NML Cyg, a highly evolved OH/IR supergiant deeply embedded in a dusty envelope, is one of the brightest infrared objects and among the most luminous supergiants in the Galaxy. Our diffraction-limited (73 mas resolution) K-band observations of NML Cyg obtained with the SAO 6 m telescope resolved the dust formation zone of its wind for the first time.

To quantitatively interpret our images, the 11 μm visibilities, and the observed SED of NML Cyg, we performed radiative transfer modeling of the object (Fig. 9). The observations could not be fitted with a single dust envelope. To simultaneously fit observations at various wavelengths, we have to assume that at least two enhanced mass-loss episodes (superwinds) with densities higher by an order of magnitude had occurred in the past. In the near IR, the dust condensation zone is limb-brightened (see Fig. 9). For an assumed distance of 1 kpc, the model predicts a stellar luminosity of $10^5\,L_\odot$ and a current mass-loss rate of $10^{-4}\,M_\odot\,\mathrm{yr}^{-1}$. Our model suggests that the most recent superwind episode began half a century ago and lasted $\sim$ 20 yr, whereas the older superwind dates more than 500 yr back.

2.3 WR118: Observations and Modeling of a Wolf-Rayet Star

WR 118 is a highly evolved, carbon-rich Wolf-Rayet star with a significant IR excess produced by its dusty envelope. We performed the first diffraction-limited speckle interferometric

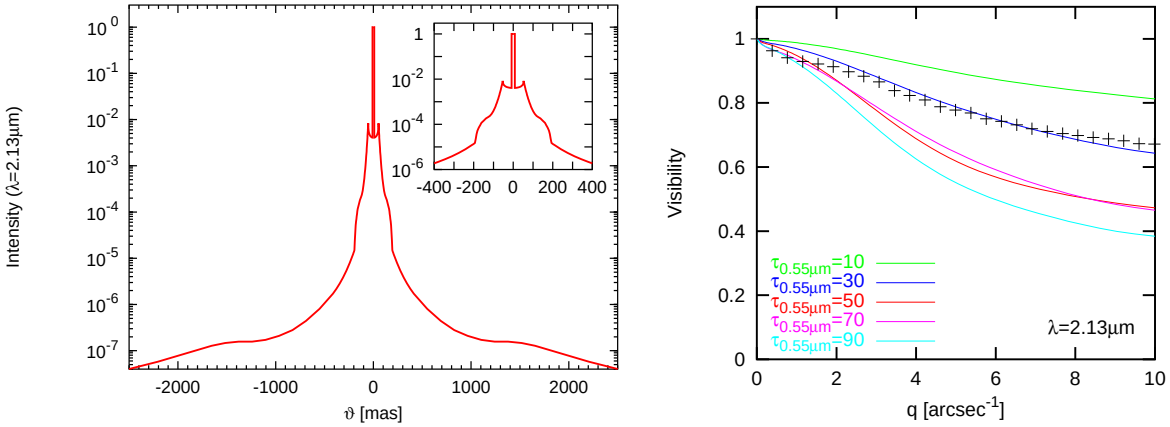

Figure 9: *Left:* Normalized K-band model intensity profile of NML Cyg with an inner superwind shell extending from 130 to 180 mas. *Right:* Comparison of the model visibilities for different optical depths with observations (crosses). The temperatures of the stellar surface and of the inner dust boundary were fixed at 2500 K and 1000 K, respectively.

observations of this object ($\lambda \sim 2.13\,\mu$m, 73 mas resolution, SAO 6 m telescope, see Fig. 10). The observed two-dimensional visibilities do not show any substantial deviation from circular symmetry. Our radiative transfer model of WR 118 fitted both its SED and K-band visibility with a spherical dusty envelope (Fig. 10). A good match was found for a distribution of dust grains with radii between 0.005 and 0.6 μm. At a distance of $\sim$ 2 kpc, the model predicts a stellar luminosity of $\sim 6 \times 10^4\,L_\odot$ and that the dust formation zone is located at a distance of 17 mas from the star ($150\,R_\star$). Assuming a wind velocity of 1200 km s^{-1}, the dust formation rate is $10^{-7}\,M_\odot$ yr^{-1}.

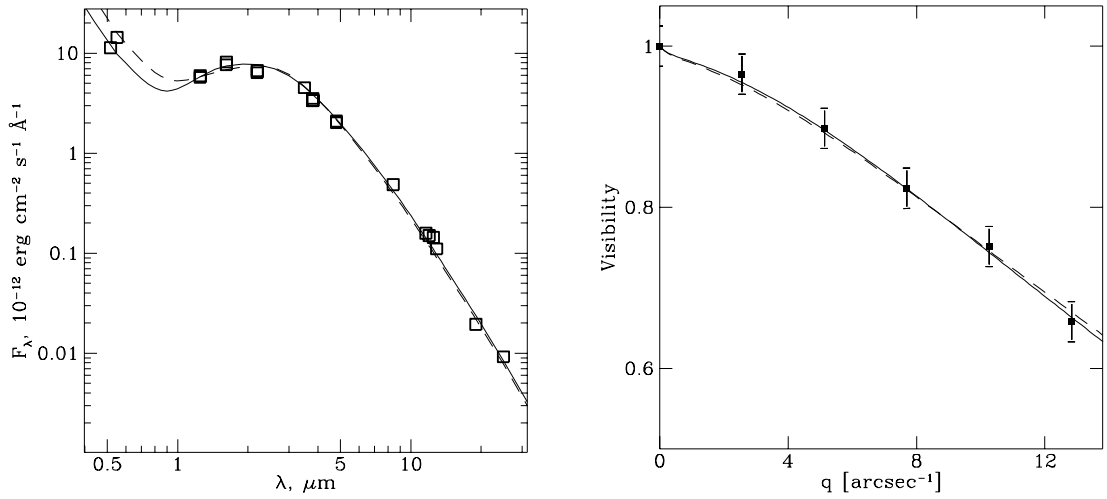

Figure 10: *Left:* Observed optical and infrared flux distribution of WR 118. Data points are shown as open squares. *Right:* Visibility of WR 118 at 2.13 μm. The observations are shown as filled squares. The two curves are fits based on two of our radiative transfer models.

2.4 MWC 349A: A Supergiant or a Pre-Main Sequence Star Surrounded by a Dust Disk ?

Figure 11 shows our bispectrum speckle interferometric studies of MWC 349A, a peculiar object with a strong IR excess and extremly strong emission lines.

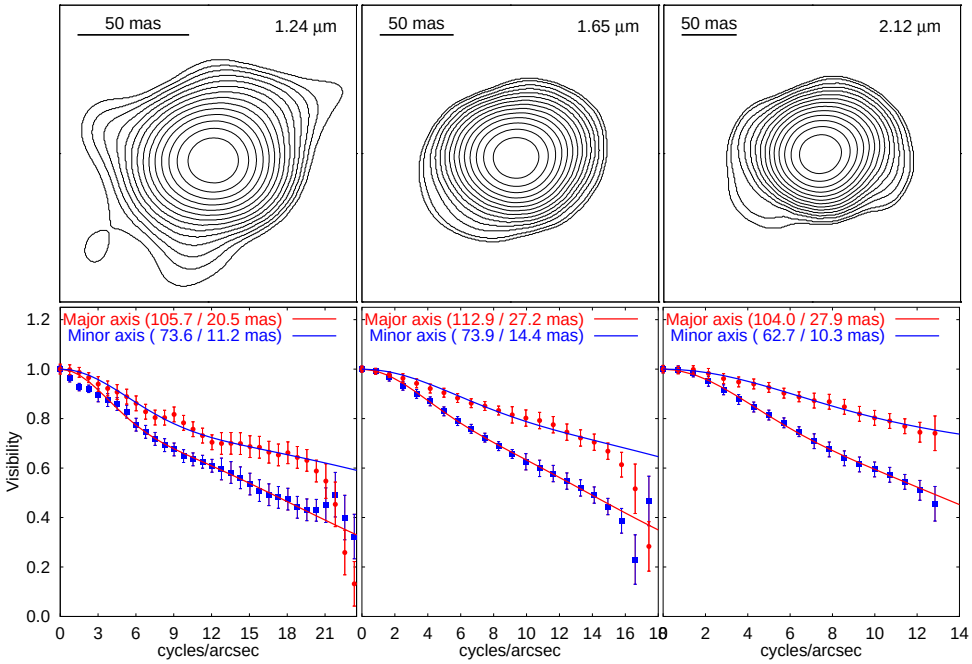

Figure 11: *Top*: Contour plots of the reconstructed images of MWC 349A at near-IR wavelengths. *Bottom*: Cuts through the observed 2D visibilities along the major and minor axis and comparison with our two-component elliptical uniform-disk models.

MWC 349A was considered a pre-main sequence object, mainly due to the presence of a bipolar nebula and possibly a disk, inferred from high levels of polarization and double-peaked emission-line profiles. Our diffraction-limited J-, H-, and K-band images with resolutions of 43–74 mas suggest that the star is embedded in a disk-like structure seen almost edge-on. The visibility shows a two-component structure; for example, the sizes of the two disk components in the H band are $\sim 170 \times 70$ mas and 27×15 mas. The observed disk sizes are consistent with the theoretical predictions for the inner and outer dimensions of photoevaporating accretion disks around young stars reported by Hollenbach et al. (1994). However, our study demonstrates that the classification of MWC 349A as a pre-main sequence star or a young planetary nebula is problematic. Our analysis of its basic parameters suggests that MWC 349A is either a B[e] supergiant or a binary system, where the B[e] companion dominates the observed properties.

2.5 CIT 3: An Oxygen-Rich AGB Star Inside a Dense Dusty Envelope

CIT 3 is an oxygen-rich AGB star pulsating with a period of 660 days and located at a distance of ~ 650 pc. Its surface is being eroded by a strong stellar wind with a current mass-loss rate close to $10^{-5}\,M_{\odot}\,\mathrm{yr}^{-1}$. CIT 3 is one of the brightest infrared sources on the sky. Our first near-infrared bispectrum speckle interferometry with the SAO 6 m telescope allowed the reconstruction of J-, H-, and K-band images with diffraction-limited resolutions of 48, 56, and

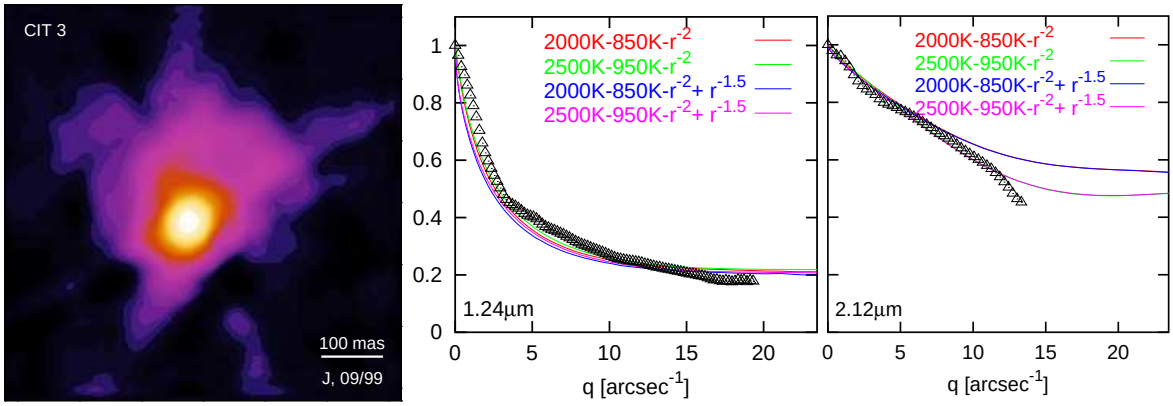

Figure 12: *Left*: J-band image of CIT 3 with 48 mas resolution. *Right*: Comparison of J and K model visibilities with observations (triangles). Different models are parameterized by stellar effective temperature, dust temperature at the inner boundary, and by density profiles $\rho \propto r^{-2}$ and $\rho \propto r^{-1.5}$.

73 mas, respectively. Although CIT 3 appears almost spherically-symmetric in H and K, its J image is clearly elongated (Fig. 12). Two distinct structures can be identified at this wavelength: a compact elliptical core with a size of $\sim$ 100 mas and a fainter, fan-shaped structure.

Our radiative transfer model fits the SED and near-infrared visibilities of CIT 3 at several wavelengths. The model implies a stellar effective temperature of 2250 K and an optically thick dusty envelope ($\tau_V \approx 30$), with the dust formation zone located at 6.6 $R_\star$ (36 mas). Furthermore, our model suggests a broken power-law density profile with $\rho \propto r^{-2}$ in the inner parts and $\rho \propto r^{-1.5}$ in a more distant region ($r > 140\,R_\star$). Assuming a constant outflow velocity, the density distribution might indicate changes of the mass-loss rate. With a typical velocity of 20 km s^{-1}, the changes occurred about a century ago. Our model predicts the current mass-loss rate to be $\sim 10^{-5}\,M_\odot\,\mathrm{yr}^{-1}$.

2.6 The Carbon Star IRC+10216: Dynamic Evolution of the Inner Dust Envelope

IRC+10216 is the nearest carbon star and the brightest object on the sky at 12 μm outside the solar system. Its very high mass-loss rate, long pulsation period (649 days), and carbon-rich chemistry suggest a very advanced stage of its AGB evolution. Our program of near-infrared bispectrum speckle interferometry of IRC+10216 with the SAO 6 m telescope now covers 8 epochs between 1995 and 2001, and reveals spectacular developments in the innermost region of its complex dusty envelope on time scales of a few months (Fig. 13).

In 1995 we discovered that the subarcsecond environment of IRC+10216 consist of 4 peaks, which we called components A, B, C, and D, in the order of their decreasing brightness (Figs. 13, 14). The components displayed significant brightness variations and fast relative motion. For example, the separation of A and B almost doubled in just 5 years. The most important question is whether we see the carbon star in the images and, if so, which component it is. To understand what goes on in IRC+10216 and to interpret the complex motions of the components A, B, C, and D, we utilized our two-dimensional radiative transfer code, as discussed in the following section. The model shows that, contrary to intuitive perception, the star is located at the position of the fainter component B. Our images now cover more than 3 pulsation periods, demonstrating that the observed structural variations are not related to the stellar pulsation cycle in a simple way. What we see in Figs. 13 and

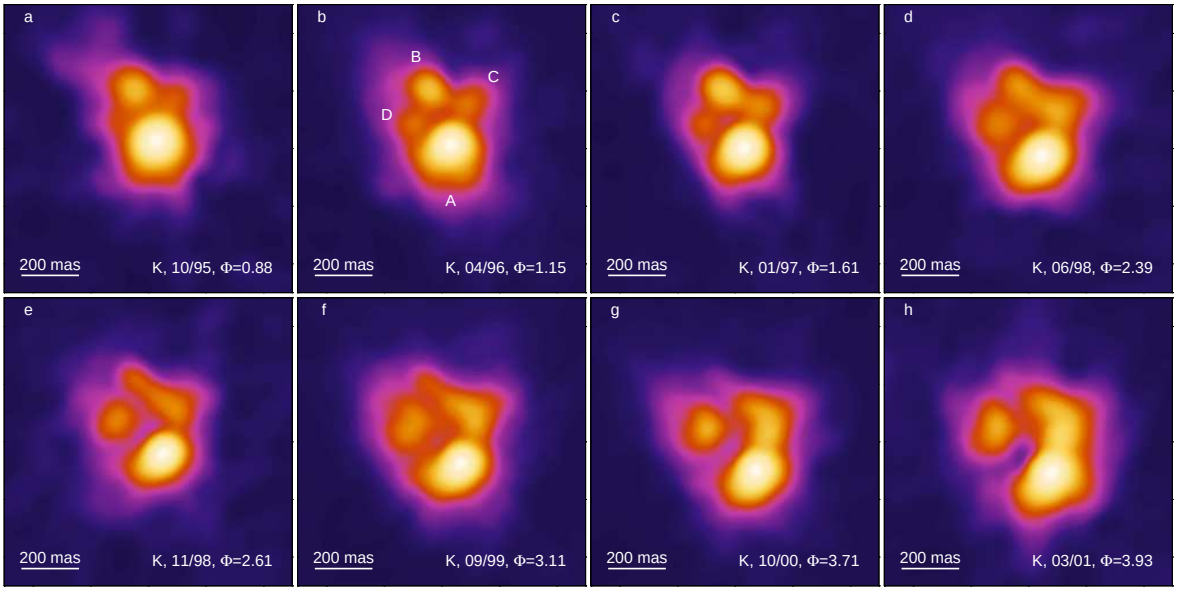

Figure 13: Evolution of the dusty envelope of IRC+10216 in our series of diffraction-limited K-band speckle images obtained with SAO 6 m telescope over 5.4 years (1995–2001). The apparent separation of the initially brightest components A and B increased from 190 to 350 mas. Component B almost disappeared in 2000, whereas the faint components C and D became relatively brighter.

14 is the effect of optical depth variations caused by increased mass loss and by new dust condensation in the optically thick, non-spherical bipolar stellar wind.

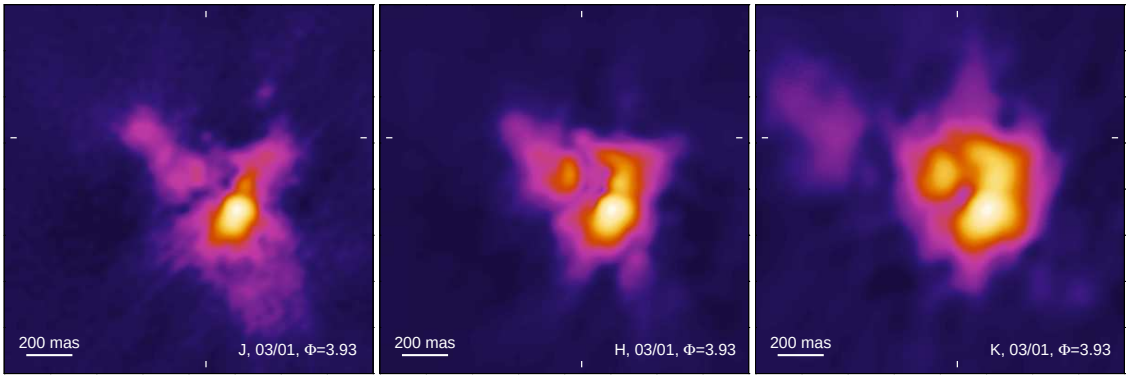

Figure 14: March 2001 images of IRC+10216 in J, H, and K bands (50, 56, and 73 mas resolution). The J-band image is dominated by dust scattering, whereas the H- and K-band images show a progressively stronger contribution of hot dust emission from the dust formation zone. The small tick marks indicate the likely position of the central star.

2.7 IRC+10216: Self-Consistent Two-Dimensional Radiative Transfer Modeling

Our previous two-dimensional radiative transfer modeling of IRC+10216 allowed us to derive its physical properties at the epoch of January 1997. Reproducing a very large number of observational constraints, the detailed model showed that the brightest peak A is radiation emitted and scattered in the optically thinner cavity of the dense circumstellar shell, while

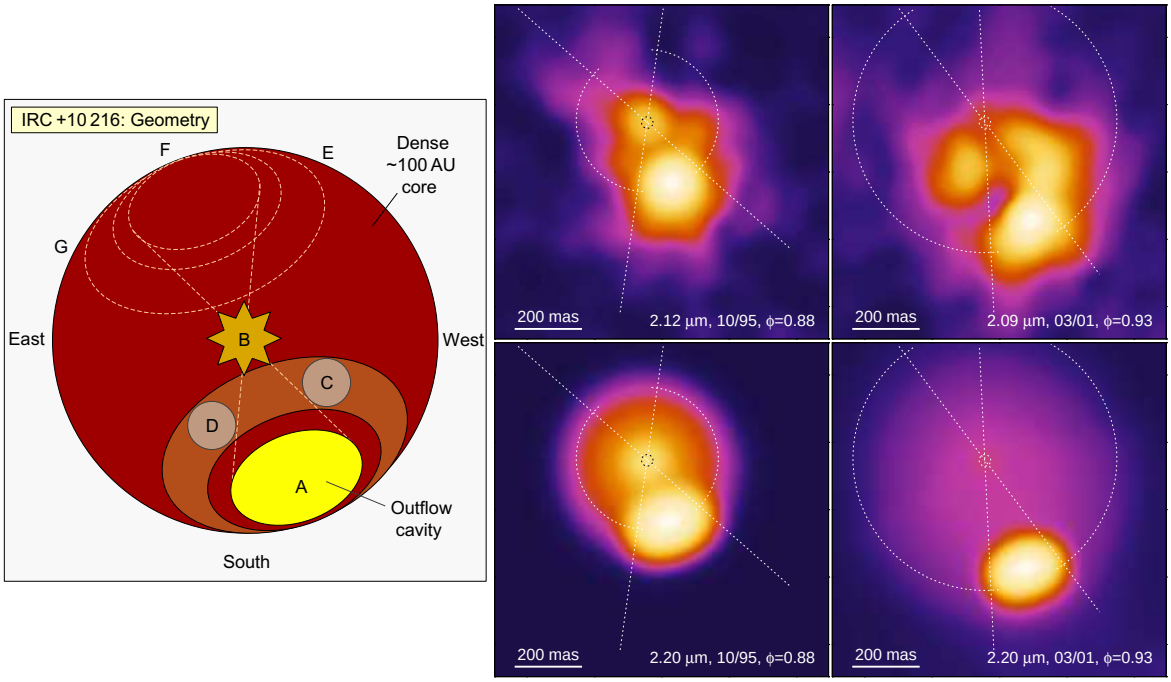

Figure 15: *Left:* Model geometry of the innermost environment of IRC+10216. *Right:* Comparison of the observed images from October 1995 and March 2001 (*top*) with our model K-band images computed for the same epochs (*bottom*). The dashed circular segments show the density peak position in the dust formation zone of our model. The small dashed circles indicate the position and size of the star (component B).

the star is actually located at the position of the second brightest component B. Having then observed the complex changes in the innermost shell over 5.4 years, we incorporated these time-dependent constraints into our new modeling to understand better the physical reasons for the observed changes (Fig. 15). One interesting question is whether we see the real motion of the dusty wind material or just the apparent shift of the dust emission spot.

The new modeling reproduces the evolutionary constraints quite well, implying the following physical picture. During the last 50 years, we have been witnessing an episode of steadily increasing mass loss from the central star, from $10^{-5} M_{\odot}\,\mathrm{yr}^{-1}$ to the high rate of $3 \times 10^{-4} M_{\odot}\,\mathrm{yr}^{-1}$ in 2001. The rapid increase of the mass loss of IRC+10216 and continuing time-dependent dust formation and destruction caused the observed displacement of the initially faint components C and D and of the bright cavity A from the star (component B), which almost disappeared in our images in 2001. Increasing dust optical depths are causing strong backwarming which leads to higher temperatures in the dust formation zone. This is displacing the latter outward with a velocity 27 $\mathrm{km\,s}^{-1}$ due to the evaporation of the recently formed dust grains. This self-regulated shift of the dust density peak in the bipolar shell mimics a rapid radial expansion, whereas the actual outflow probably has a speed lower than 15 $\mathrm{km\,s}^{-1}$.

2.8 IRC+10216: Time-Dependent Dust Formation in a Dense Stellar Wind

If the star is located at the position of component B, as suggested by our two-dimensional radiative transfer modeling (Sect. 2.7), its decreasing brightness may be caused by the continuing formation of new dust in the stellar wind. To investigate whether such a scenario could

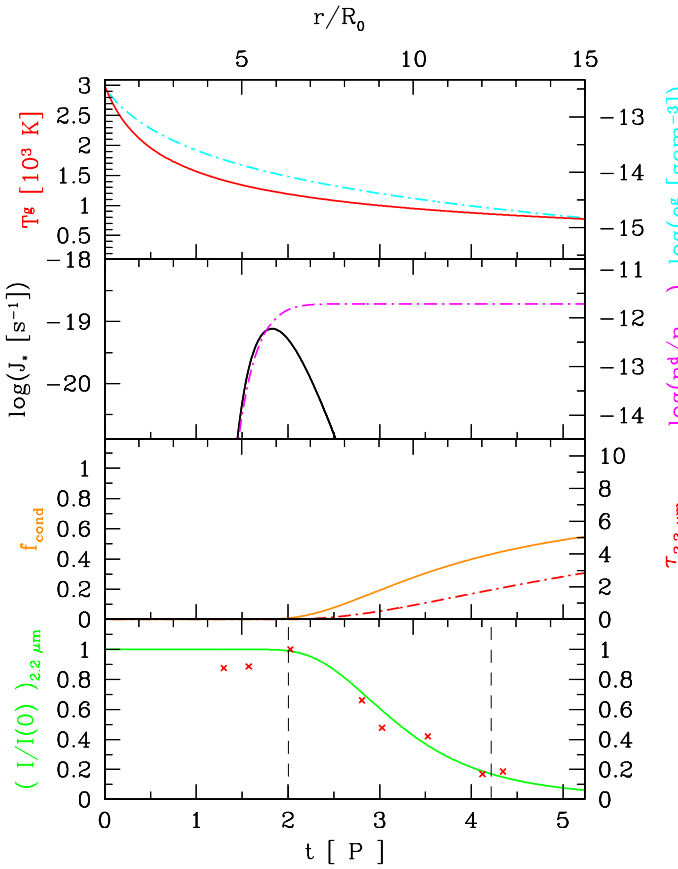

Figure 16: Evolution of the gas box (time t is in units of the period $P = 649\,\mathrm{d}$). In the panels from top to bottom, we show gas temperature and density, dust nucleation rate J_* and number of dust grains per hydrogen nucleus, degree of dust condensation f_{cond} and optical depth at $2.2\,\mu\mathrm{m}$, and finally the normalized emergent intensity at $2.2\,\mu\mathrm{m}$ compared to the observed intensity of component B (crosses, also normalized to its maximum). To describe the changing thermodynamic conditions in the gas element, we assume power-laws $T \propto r^{0.5}$ and $\rho \propto r^{-2}$ for the gas temperature and density distributions. Parameters adopted: gas temperature 3000 K at radius $3 \times 10^{13}\,\mathrm{cm}$, stellar luminosity $1.5 \times 10^4\,L_\odot$, mass-loss rate $10^{-4}\,M_\odot \mathrm{yr}^{-1}$, outflow velocity of $15\,\mathrm{km\,s}^{-1}$, and carbon-to-oxygen abundance ratio of 1.5 (by number).

explain the observed time scale of the fading of component B, we constructed a simple gas box model to follow the process of carbon grain formation in a gas element moving away from the star at a constant wind velocity. We considered heteromolecular formation and growth of carbon grains, including reactions with C, C_2, C_2H, and C_2H_2. The number densities of the relevant hydrocarbon molecules were obtained by assuming chemical equilibrium in a carbon-rich gas with otherwise solar abundances. To calculate the extinction coefficient of amorphous carbon grains, we applied the small particle limit of Mie theory. Our results, shown in Fig. 16, confirm that dust formation in front of the star can indeed reproduce the observed time scale of the fading of component B for realistic values of the model parameters. This implies that the current mass-loss rate of IRC+10216 must have increased considerably above the canonical value of $\sim 10^{-5} M_\odot\,\mathrm{yr}^{-1}$ derived from CO line observations of more distant and, therefore, older parts of the circumstellar envelope.

2.9 Stellar Evolution Calculations

Our detailed calculations cover all phases of stellar evolution, from the pre-main sequence stages to the white dwarf domain, with the main emphasis on the AGB stars and their descendants. Expertise in stellar evolution has proven to be very useful for the interpretation of our high-resolution images probing the innermost regions of circumstellar envelopes and even resolving stellar surfaces. For example, the masses, luminosities, and effective temperatures derived from our detailed models of the Red Rectangle (Sect. 2.1) and IRC+10216 (Sect. 2.7) have to be compared with the predictions of stellar evolution theory.

The evolution of AGB stars is governed by the recurrent thermal instabilities of the helium burning shell (thermal pulses), the convective envelope's penetration into the hydrogen

burning shell (hot bottom burning), and steeply increasing mass loss leading to the formation of dusty circumstellar envelopes. Important consequences of the thermal pulses are the mixing of interior carbon and s-process elements toward the surface (3rd dredge-up) and the formation of carbon stars (Fig. 17). We enhanced our stellar evolution code with some extra partial mixing (overshooting) beyond the classical convective border, based on hydrodynamical studies of convection. For AGB stars with rather small core masses of $\sim 0.6\,M_\odot$, this provides both a sufficiently strong 3rd dredge-up to explain carbon stars and the production of the neutron source ^{13}C as required by observations. Whether the carbon stars are eventually formed depends on the efficiency of the 3rd dredge-up and on the outcome of the competition with hot bottom burning.

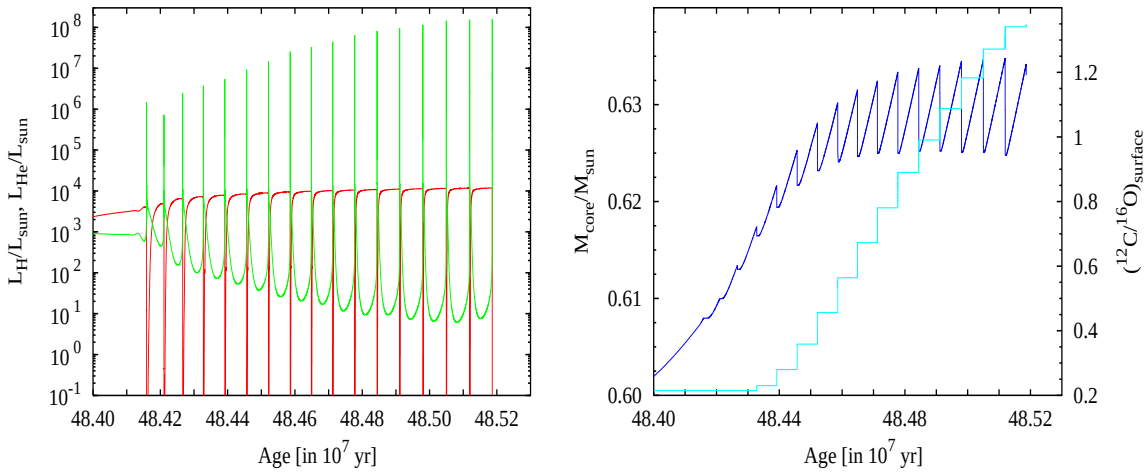

Figure 17: Birth of a carbon star with $M_{\rm init} = 3\,M_\odot$ on the AGB. *Left:* Evolution of hydrogen (red) and helium (green) luminosities. *Right*: Evolution of the mass of the hydrogen-exhausted core (dark blue) and surface abundance ratio ^{12}C/^{16}O (cyan). The peaks in $L_{\rm He}$ and the corresponding fading of $L_{\rm H}$ are caused by the thermal pulses of the helium burning shell. The star becomes a carbon star (C/O > 1) after ~ 13 thermal pulses and the accompanying 3rd dredge-up events.

Current stellar evolution theory has difficulty in explaining the nature of hydrogen-deficient post-AGB stars. To better understand this class of objects, we computed the evolution of post-AGB stars in which the chemical composition of the stellar surface changes from hydrogen-rich to strongly hydrogen-deficient due to a very late thermal pulse (born-again scenario). These models were the first to achieve general agreement with the surface abundance pattern observed in the hydrogen-deficient stars. Recent development of our numerical evolutionary code allowed us to study the effects of rotation on the stellar structure and evolution, including the angular momentum transport and different rotational mixing processes. In the future, we will focus on the evolution of rotating AGB and post-AGB stars, since the influence of rotation on these evolutionary stages is only poorly understood.

People involved: T. Blöcker, T. Driebe, K.-H. Hofmann, N. R. Ikhsanov, A. B. Men'shchikov, K. Ohnaka, D. Schertl, G. Weigelt, J. M. Winters

Collaborations: I. I. Balega, Y. Y. Balega (Special Astrophysical Observatory, Russia); W. C. Danchi (NASA Goddard Space Flight Center, USA); A. S. Miroshnichenko (University of Toledo, USA); J. D. Monnier (Smithsonian Astrophysical Observatory, USA); P. G. Tuthill (University of Sydney, Australia); B. F. Yudin (Sternberg Astronomical Institute, Russia); L. R. Yungelson (Institute of Astronomy, Russia).

3 First K- and H-Band Images of the 22 × 40 mas NIR Core of the Seyfert Galaxy NGC 1068

In 1996 we resolved the infrared core of NGC 1068 for the first time. A diffraction-limited image with a resolution of 76 mas was reconstructed from our 6 m telescope speckle interferograms using our bispectrum speckle interferometry method. The visibility function and the image showed that the azimuthally averaged diameter of the resolved core is ∼ 30 mas, or ∼ 2 pc. During the last three years we were able to obtain more *K*-band as well as *H*-band speckle interferograms. From these interferograms we reconstructed an improved *K*-band and the first *H*-band image of the infrared core of the Seyfert galaxy NGC 1068. The two-dimensional visibilities and the images (Fig. 18) show that the dominant 30 mas object is elongated (extension at P.A. ∼ 340°) and has a *K*-band size (FWHM Gaussian diameter) of 22 × 40 mas or ∼ 1.6 × 3 pc and an *H*-band size of ∼ 18 × 45 mas. Furthermore, the visibility

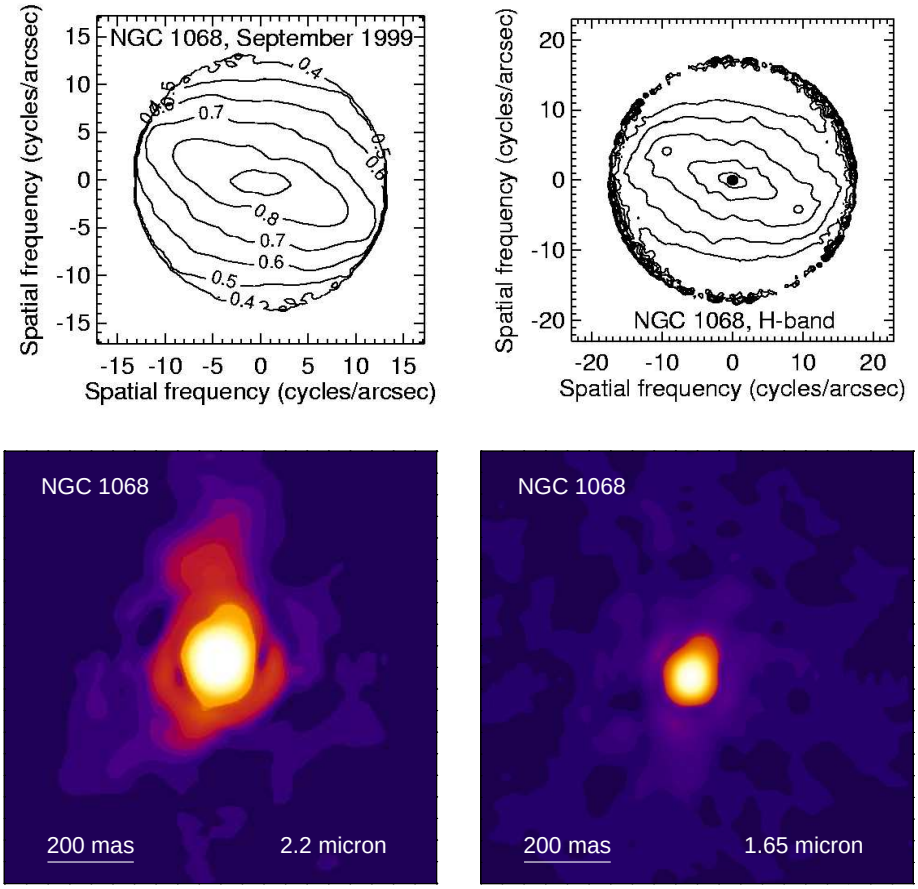

Figure 18: Bispectrum speckle interferometry of NGC 1068 (SAO 6 m telescope): *Top:* *K*-band visibility (right), *H*-band visibility (left). *Bottom:* *K*-band image with 76 mas resolution (left), *H*-band image with 57 mas resolution (right).

value at the diffraction cut-off frequency allows the determination of an upper limit for the *K*-band flux from an unresolved component. The position angle of the 22 × 40 mas object is ∼ 160°/340° . Therefore, the 22 × 40 mas NIR object is neither aligned with the VLBA disk at position angle ∼ 106 degree (angular size ∼ 5 × 40 mas) discovered by Gallimore et al.

(1997) nor with the position angle of the inner radio jet. The 1.6×3 pc object is probably caused by dust located above the torus (as predicted by radiative transfer models) or by dust at the western surface of an outflow cavity. This dust emits thermal K-band light and scatters K-band light emerging at the central continuum source or at the inner edge of the torus.

Two-dimensional radiative transfer modeling is planned for the detailed interpretation of the observations (using a code similar to that discussed in the Red Rectangle section). Currently, we are reducing Keck data which allows the reconstruction of the elongated object (P.A. $\sim 340°$) with unprecedented resolution – 4 times higher than that of the Hubble Space Telescope. The first observations of NGC 1068 with the VLTI interferometer will be carried out next year during our VLTI AMBER guaranteed observing time. AMBER is the near-infrared phase-closure instrument of the VLTI. The VLTI AMBER observations will allow us to study active galactic nuclei with an unprecedented NIR resolution of 1 mas and a spectral resolution of 10 000.

People involved: K.-H. Hofmann, D. Schertl, G. Weigelt, M. Wittkowski

Collaborations: Y. Balega (SAO); T. Beckert (Harvard); W. Duschl (Univ. Heidelberg)

4 Infrared Long-Baseline Interferometry

4.1 A New Type of JHK-Band Beam Combiner for the IOTA IR Long-Baseline Interferometer: Spectro-Interferometry of T Cep

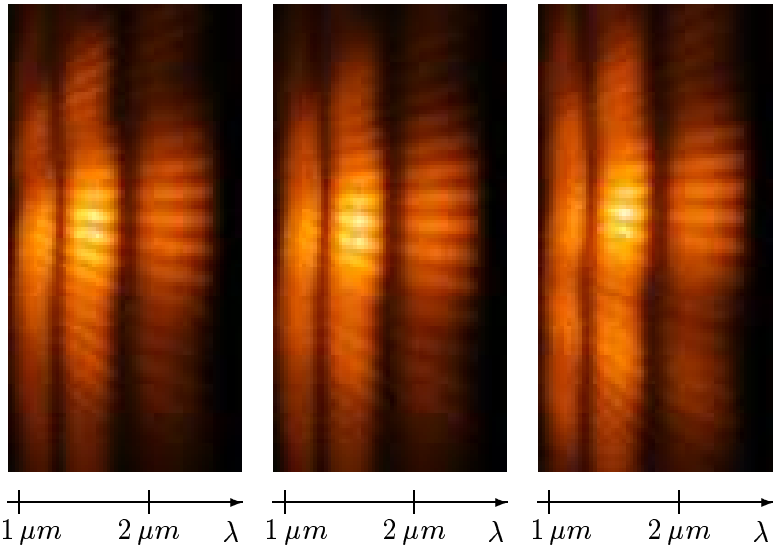

Figure 19: Three consecutive JHK-band IOTA interferograms of T Cep (wavelength range 1 – 2.3 μm from left to right in each panel).

Our new JHK-band (1.0 to 2.3 μm) beam combiner instrument allows the *simultaneous* recording of spectrally dispersed J-, H-, and K-band Michelson interferograms. The optics of this beam combiner consists of an anamorphic cylindrical lens system and a prism. Using this beam combiner, we carried out observations of the Mira variable T Cep with the Infrared Optical Telescope Array (IOTA) at 4 different baselines in the range of 14 to 27 m. From the

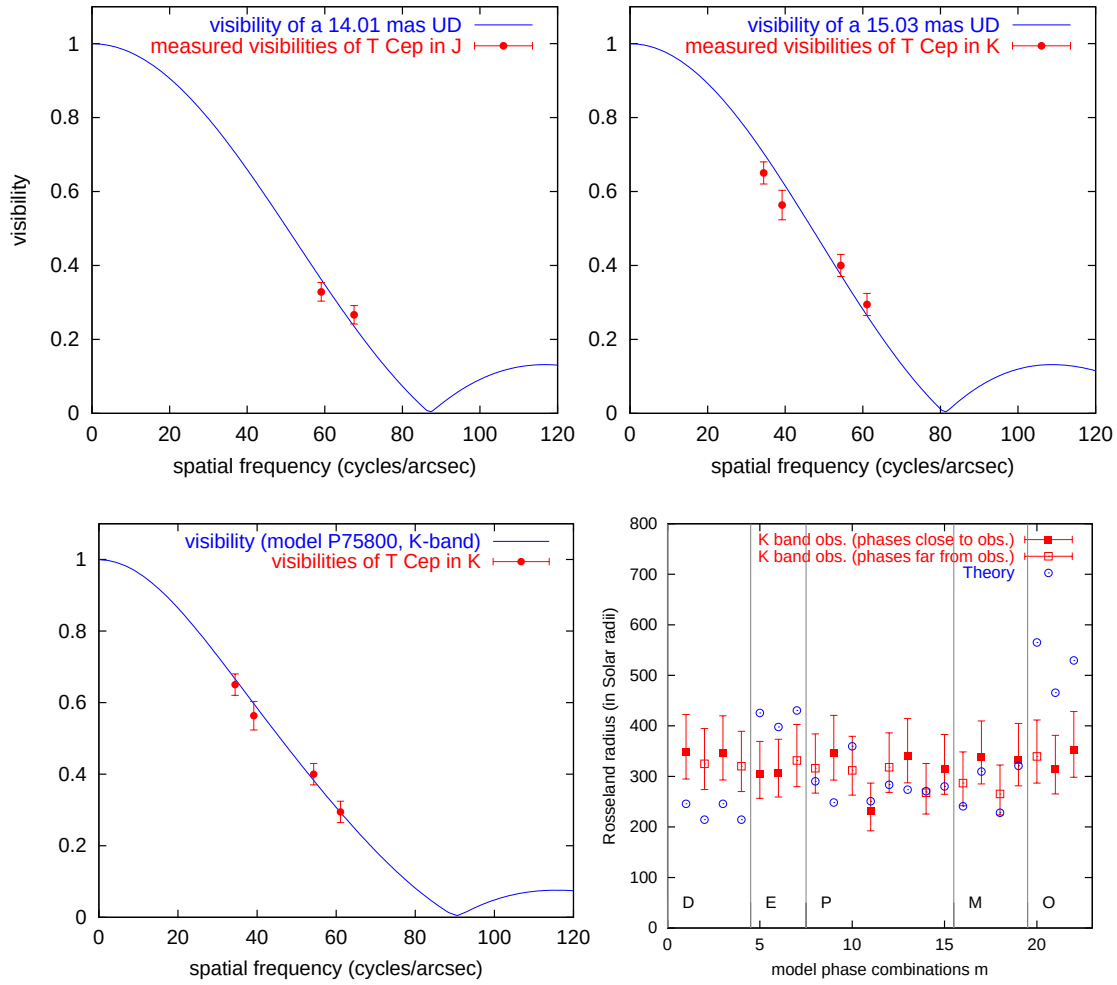

Figure 20: *Top:* Uniform-disk fits to the visibilities of T Cep measured in the J- and K-bands. *Bottom:* Fit of the model CLV of the best-fitting fundamental mode model P75800 to the measured K-band visibilities of T Cep (left). Comparison of linear T Cep Rosseland radii derived from the observations with theoretical Bessel-Scholz-Wood model radii. Different m-values correspond to different models, phases, and cycles (right).

spectrally dispersed interferograms of T Cep (see Fig. 19) we derived the visibilities and the J-, H-, and K-band uniform-disk diameters of 14.0 mas, 13.7 mas, and 15.0 mas, respectively (Fig. 20). Furthermore, angular stellar filter radii and Rosseland radii were calculated by fitting the measured visibilities with theoretical center-to-limb intensity variations (CLVs) predicted from different Bessel-Scholz-Wood models. Combining the angular Rosseland radii derived from our K-band visibilities and the HIPPARCOS parallax (4.76 mas), we determined the linear Rosseland radius of T Cep to be 329^{+70}_{-50} $R_\odot$ (the error bars are dominated by the parallax error). The comparison of the measured stellar parameters (e.g., diameters, effective temperature, visibility shape) with theoretical parameters indicates whether any of the Bessel-Scholz-Wood models (D, E, P, M, or O model; see Fig. 20, lower right) is a fair representation of T Cep. The above Rosseland radius turns out to be in good agreement with the theoretical value of 315 $R_\odot$ predicted by the M-model of the Bessel-Scholz-Wood models.

The ratios of visibilities of different spectral channels can be measured with higher precision than absolute visibilities can. Therefore, we used the visibility ratios $V(\lambda_1)/V(\lambda_2)$ to

investigate the wavelength dependence of the stellar diameter of T Cep. We find that at 2.03 μm the uniform-disk diameter of T Cep is 1.26 times larger than at 2.26 μm. The larger angular diameter at 2.03 μm can be attributed to the absorption bands of H_2O, where we see the upper layers of the atmosphere in contrast to the continuum at 2.26 μm. The measured diameter ratios are in good agreement with the ratios predicted by recent theoretical models.

4.2 IOTA IR Long-Baseline Interferometry of the Symbiotic Star CH Cyg

Symbiotic stars are close binary systems consisting of a cool red giant and a hot star. Interaction between both components can lead to accretion phenomena and highly variable light curves. CH Cyg, which is a luminous triple symbiotic system, is one of the best studied objects of this class of stars, and exhibits very complicated photometric and spectroscopic behavior. We carried out observations of CH Cyg with our new JHK-band beam combiner mounted on the IOTA interferometer (baselines 17 - 25 m).

First, we derived uniform-disk diameters from the observed J-, H-, and K-band visibility functions. For example, a uniform-disk fit to the H-band visibilities gives a stellar diameter of 7.8 mas (see Fig. 21). Then we applied the same method as described in Sect. 4.1, in order to determine angular stellar filter radii and Rosseland radii. Combining these angular Rosseland radii and the HIPPARCOS parallax, we derived the linear Rosseland radii to be between 214 and 243 $R_\odot$ (Fig. 21). These values agree well, within the error bars, with the theoretical values of 230 to 282 $R_\odot$, which are predicted from the fundamental mode pulsator models. The first overtone pulsator models turn out not to be in good agreement with the observations. We also found that the uniform-disk diameter at 2.03 μm is ~1.1 times larger than those at 2.15 μm and 2.26 μm. As in the case of T Cep, the larger angular diameter at 2.03 μm can be attributed to the absorption bands of H_2O.

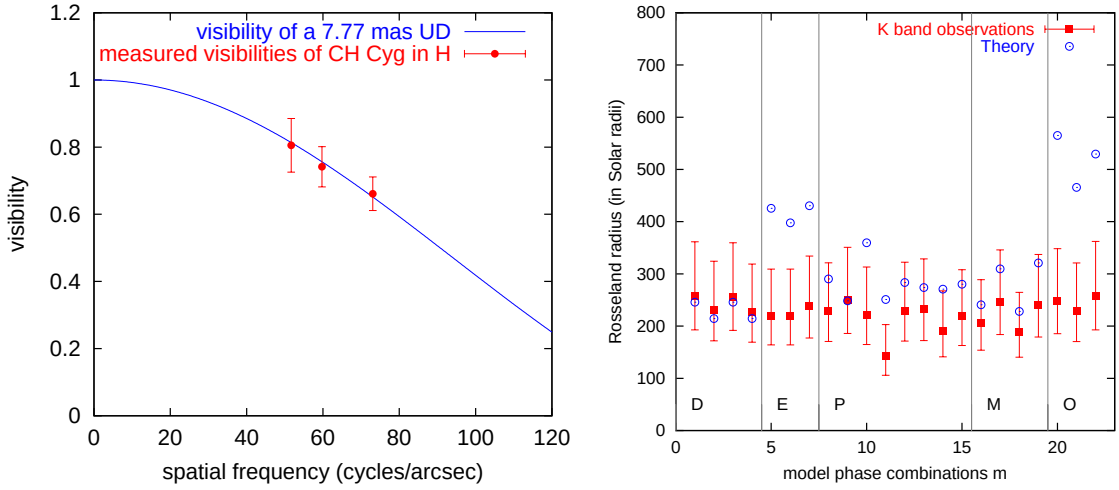

Figure 21: *Left:* Uniform-disk fit to the H-band visibilities of CH Cyg. *Right:* Comparison of linear Rosseland radii derived for CH Cyg with theoretical radii. Different values of m correspond to different models, phases, and cycles.

4.3 IOTA Interferometry of the Circumstellar Environment of R CrB

R CrB stars are characterized by irregular sudden declines in their visual light curves as deep as $\Delta V \sim 8$. This is attributed to the occasional ejection of dust clouds in random directions, with the deep minima caused by clouds ejected along the line of sight. However, the effective temperatures of R CrB stars are as high as 7000 K and the mechanism of dust formation in such a hostile environment is not fully understood.

We performed the first long-baseline interferometric observations of R CrB with IOTA, using our new JHK beam combiner. The circumstellar envelope of R CrB was resolved at a baseline of 21 m, along a position angle of $\sim 170°$, and the visibilities in the J-, H-, and K-bands are 0.97, 0.78, and 0.61, respectively. The visibilities obtained with IOTA, as well as visibilities which we obtained by speckle interferometry with the SAO 6 m telescope, and the spectral energy distribution were fitted with two-component models consisting of the central star and an optically thin dust shell (see Fig. 22). The observed visibilities can be fitted with models which have a temperature of 950 – 1100 K and an inner boundary of 60 – 80 $R_\star$. The K-band visibilities predicted by the models are about 10% smaller than the visibility obtained with IOTA, which represents good agreement, given the simplifications adopted in our models when compared to the complexity of the source. As a hypothesis to explain the small discrepancy, we propose that there might be a group of newly formed dust clouds, which could appear as a third visibility component.

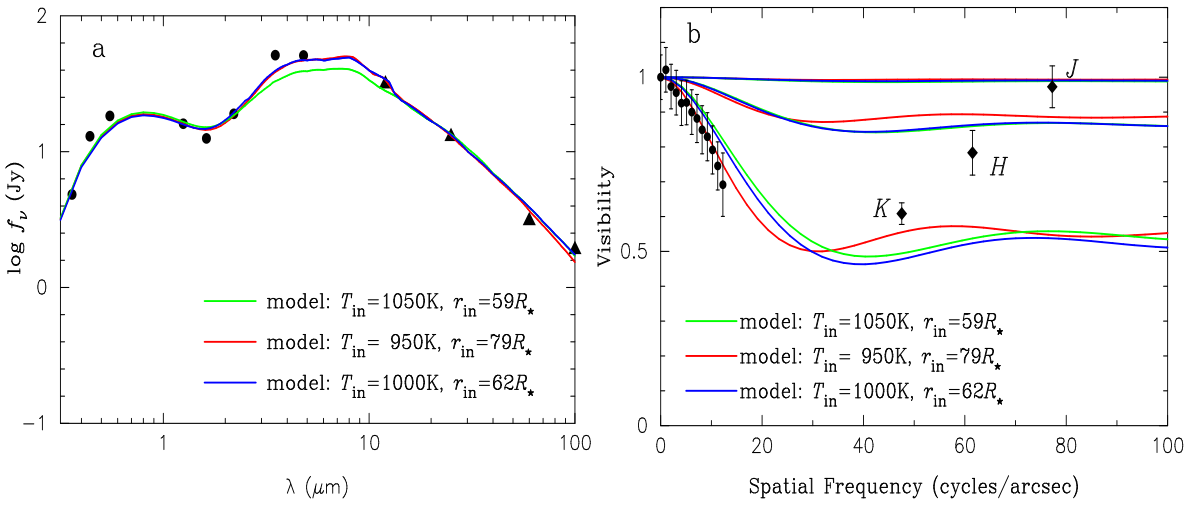

Figure 22: *a*: Spectral energy distributions of R CrB. The filled circles represent the photometric data obtained in the same period as our IOTA observations. The three curves show models calculated with different opacities of amorphous carbon. The inner radius of the dust shell and the temperature are also given for each model. *b*: Visibilities of R CrB. The filled diamonds represent the JHK-band visibilities observed with IOTA. The filled circles are K-band speckle visibilities obtained with the SAO 6 m telescope, The visibilities predicted for the JHK-bands are represented by the curves with different colors, corresponding to the models plotted in *a*.

4.4 Development of the VLTI Phase-Closure Instrument AMBER: 1 mas Resolution at the Wavelength of 1 micron

Infrared long-baseline interferometry with the ESO Very Large Telescope Interferometer (VLTI; four 8 m and three 1.8 m telescopes) and the Keck interferometer will revolutionize infrared astronomy as radio interferometry has revolutionized radio astronomy during the last few decades. The AMBER instrument is the NIR beam combiner of the VLTI. AMBER was built during the last three years by an international consortium of groups at the university of Nice, the university of Grenoble and the Arcetri Observatory, the MPIfR Infrared Technology division and our astronomical group. The MPIfR was responsible for the detector system. The integration phase started in September 2002.

The AMBER VLTI instrument is a three-telescope phase-closure instrument. At the wavelength of 1 μm and with baselines of up to 200 m, an angular resolution of 1 mas will be obtained. The AMBER fiber optics beam combiner allows the precise measurement of visibilities and closure phases. For example, visibilities can be measured with errors smaller than 0.1%. The spectrally dispersed interferograms allow the measurement of differences between visibilities at different wavelengths with errors smaller than 10^{-4}. The limiting magnitude of AMBER is expected to be $K \sim 14$.

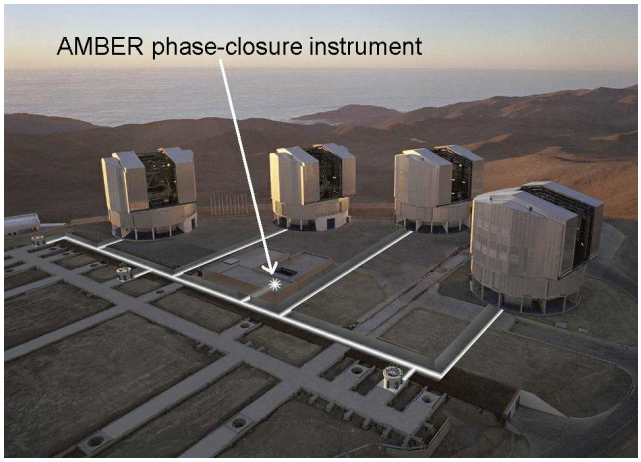

Figure 23: AMBER instrument

Our main scientific objectives are VLTI investigations of extra-solar planets, young stellar objects, evolved stars, and AGN with high spatial resolution (1 mas) and high spectral resolution of 10^2 to 10^4. The high precision of absolute visibilities and of visibility differences will very likely allow the interferometric detection of extra-solar planets and the resolution of the Broad-Line Region of AGN in the infrared wavelength region. Our first observations are planned for summer 2003 during the AMBER commissioning phase.

People involved: U. Beckmann, T. Blöcker, T. Driebe, K.-H. Hofmann, K. Ohnaka, D. Schertl, G. Weigelt

Collaborations: J.-P. Berger, M.G. Lacasse, R. Millan-Gabet, J.D. Monnier, E. Pedretti, W.A. Traub (Harvard-Smithsonian Center for Astrophysics); M.K. Brewer, F.P. Schloerb (Univ. of Massachusetts); V. Shenavrin, B. Yudin (Sternberg Astronomical Inst.; M. Scholz (Institut für Theoret. Astrophysik, Univ. Heidelberg); V. Malanushenko (Crimean Astrophys. Obs.); R. Petrov (Univ. Nice Sophia Antipolis); F. Lisi (Osservatorio Astrofisico di Arcetri); G. Duvert, L. Gluck, E. le Coarer, F. Malbet (Lab. d'Astrophysique de Grenoble).

5 Very High Energy Particles in the Universe and the Activity of Black Holes

We explore the physics of a) the origin of cosmic rays, with emphasis on the highest energies, on the one hand, and b) the physics of the activity of black holes, from stellar size black holes to the most massive black holes known in the Universe, on the other. This combination is fruitful because active black holes are prime candidates for producing very high energy particles, probably through shocks produced by their jets.

The focus of our group is centered on the partnership with the AUGER experiment, the EUSO experiment and the future studies of very high energy cosmic rays with LOFAR. AUGER is an international collaboration to build a hybrid airshower array in Argentina, with both water Čerenkov detectors and air fluorescence detectors. AUGER is the first such combined detector, and is also by far the largest such array. First events have been seen in the current development stage. EUSO is an experiment to detect air fluorescence and reflected Čerenkov radiation of airshowers from space, and is also an international collaboration. LOFAR is a giant low frequency radio array being built in the Netherlands, and is again an international collaboration. We are an official member of all three experiments. Our partnership is funded by the BMBF directly, and centered on the AUGER experiment.

We describe the work being done in three examples:

- Microquasars and high energy neutrinos
- Cosmic rays beyond 10^{15} eV, and supernova physics
- Merging of black holes, spin-flips of massive black holes, and gravitational waves

5.1 Microquasars and High Energy Neutrinos

Black holes are known today from stellar mass scales to the giant black holes, such as in the elliptical galaxy M87, at $3 \cdot 10^9$ solar masses. They exist in the centers of almost all galaxies, and their mass correlates both with the mass of the spheroidal component of the old stars, and with the velocity dispersion of the stellar population around the black holes in the central region of the galaxies. There is an additional population of stellar size black holes in binary systems, with typical masses in the range of about 5 to 10 solar masses.

In the last three years we have been able to show that the jet-disk symbiosis picture developed by us is also applicable to the binary star black hole systems. These systems are also known to exhibit an accretion disk, fed by mass transfer from the partner star, and a radio jet, which is also relativistic, and therefore they have been dubbed "microquasars".

The recent observations of microquasars with the X-ray satellite CHANDRA provided a welcome opportunity to test the physical concepts of our jet-disk symbiosis concept originally developed for more massive systems. In the last three years we have been able to show that almost the entire electromagnetic spectrum can be described by emission from the jet, and only a small part of the observed emission arises from the accretion disk, and possibly from a small disk corona. The variability and the spectrum could be matched with a simple description of synchrotron and inverse Compton emission from the jet, using shock acceleration as one key concept. The model then indicates the location of the shock and its physical parameters, as well as the phase space distribution of the energetic electrons and/or positrons. Fig. 24 shows one example for our spectral fits for a microquasar.

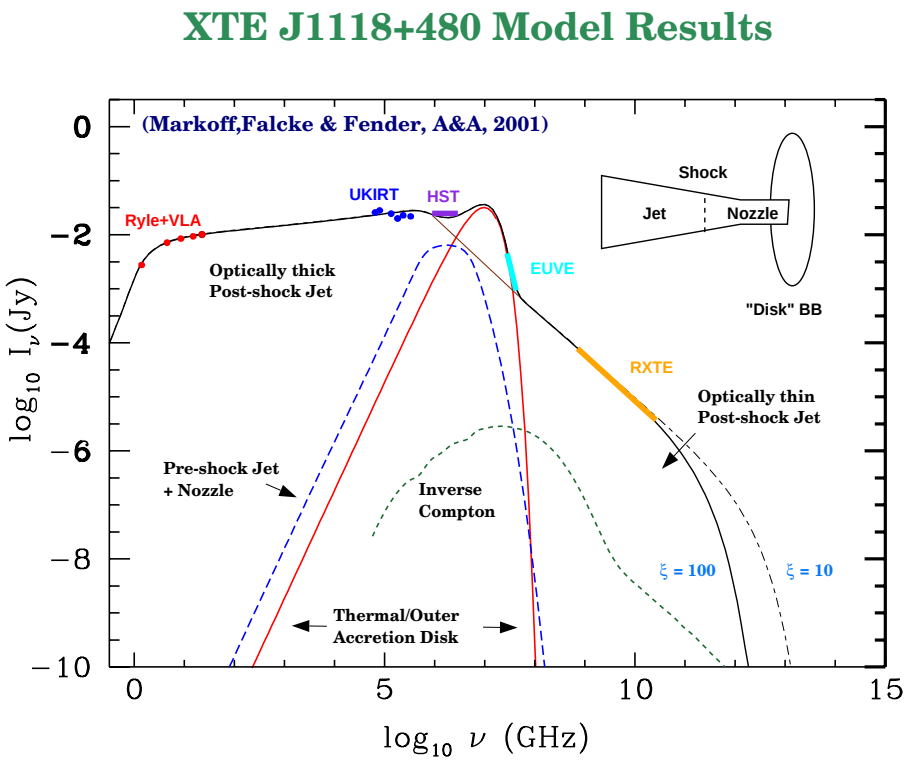

Figure 24: Our jet-disk symbiosis model fitted to the CHANDRA data, using the microquasar XTEJ1118+480 as an example; we also show the geometry of the model and give some model parameters: thermal disk inner edge: $T_d = 1.7 \cdot 10^5$ K, $L_d = 5 \cdot 10^{35}$ erg/s, $r_d = 750\, r_g$, $M_d = 0.1$; jet parameters (50% accelerated): $r_{noz} = 3$ r g, $g_j = 0.01$, $Z_{sh} = 90\, r_g$, $\Theta = 32°$, $T_e = 8 \cdot 10^9$ K.

These successful and conceptually simple fits have now been extended to low luminosity active galactic nuclei, and provide now a backbone for studying the hadronic interactions in jet-disk systems of all powers. Microquasars are now a very well-studied testbed for all processes expected to take place in very powerful sources, including high energy hadronic and leptonic processes. Similarly, Gamma Ray Bursts provide a further test for black hole formation in stellar binary systems, and also for cosmological evolution, as we have shown and continue to investigate. This work leads to the possibility to verify again our concept that radio galaxies and their cousins, the relativistic jets pointed at us such as BL Lac type sources and GHz peaked sources, provide the highest energy particles known to us in the Universe. All these emission processes are likely to involve hadronic interactions and will then be testable with very high energy neutrino observations. Fig. 25 shows the example of the Galactic center low luminosity AGN Sgr A*.

5.2 Cosmic Rays Beyond 10^{15} eV, and Supernova Physics

Cosmic rays range over energies that reach $3 \cdot 10^{20}$ eV, and show few features in their overall spectrum, see Fig. 26. Considering the complete set of all-particle data, the overall spectrum can be well described by a sequence of powerlaws, one going from 10^9 eV all the way to the "knee", at $3 \cdot 10^{15}$ eV, with a spectral index of -2.67 in number per energy bin, here visible through the overall downward curvature in Fig. 26. The second range is from this knee to the "second knee", at $3 \cdot 10^{17}$ eV, with a spectral index of about -3.1. At that energy

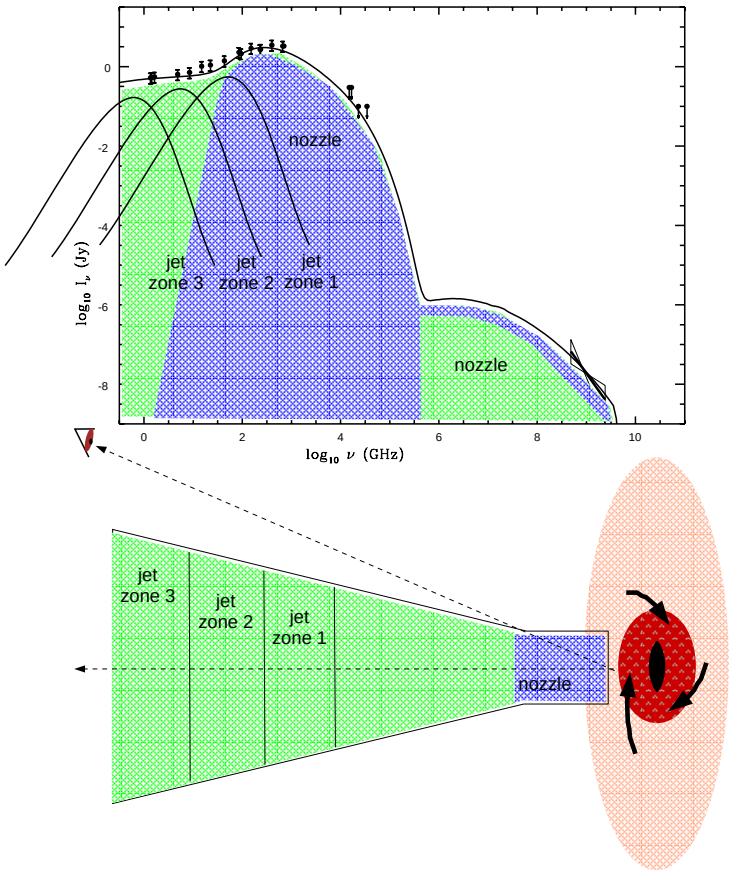

Figure 25: Our jet-disk symbiosis model fitted to the CHANDRA data, using the low luminosity active galactic nucleus in our Galaxy Sgr A* as an example; again we also show the geometry of the model.

there is a slight downturn, followed by a strong transition at $3 \cdot 10^{18}$ eV; at that energy the overall spectrum becomes much flatter again, visible in Fig. 26 as a general upturn. Beyond 10^{20} eV, not shown in the figure, there is considerable experimental uncertainty. In Fig. 26. we only show data relevant for a discussion of the various chemical elements, from KASKADE (Karlsruhe), and the higher energy data. Because of the considerable expansion of the ordinate, the scatter in Fig. 26 is large. It seems that the chemical composition becomes heavier at the knee, at $3 \cdot 10^{15}$ eV; this means that increasingly heavier nuclei like Oxygen and Carbon dominate. It also appears consistently from all datasets, but not yet with reassuring certainty, that the chemical composition changes back to a light composition at $3 \cdot 10^{18}$ eV, at the energy; this means that again Hydrogen and Helium dominate. Whether this tendency is maintained to the highest energies observed is not fully clear, but all data are consistent with this. The common interpretation is that the origin of cosmic ray particles switches from a Galactic origin to an extragalactic origin at $3 \cdot 10^{18}$ eV. It is not completely excluded that the higher energy particles are also Galactic. There is consensus in the community only as far as particles up to about 10^{14} eV are concerned; they are generally believed to arise by diffusive shock accceleration from classical supernovae, stellar explosions into the interstellar medium, or ISM-supernovae.

There is only one quantitative theory at present to account for the particles beyond 10^{14} eV, which we have proposed. This theory suggests that the particles beyond 10^{14} eV

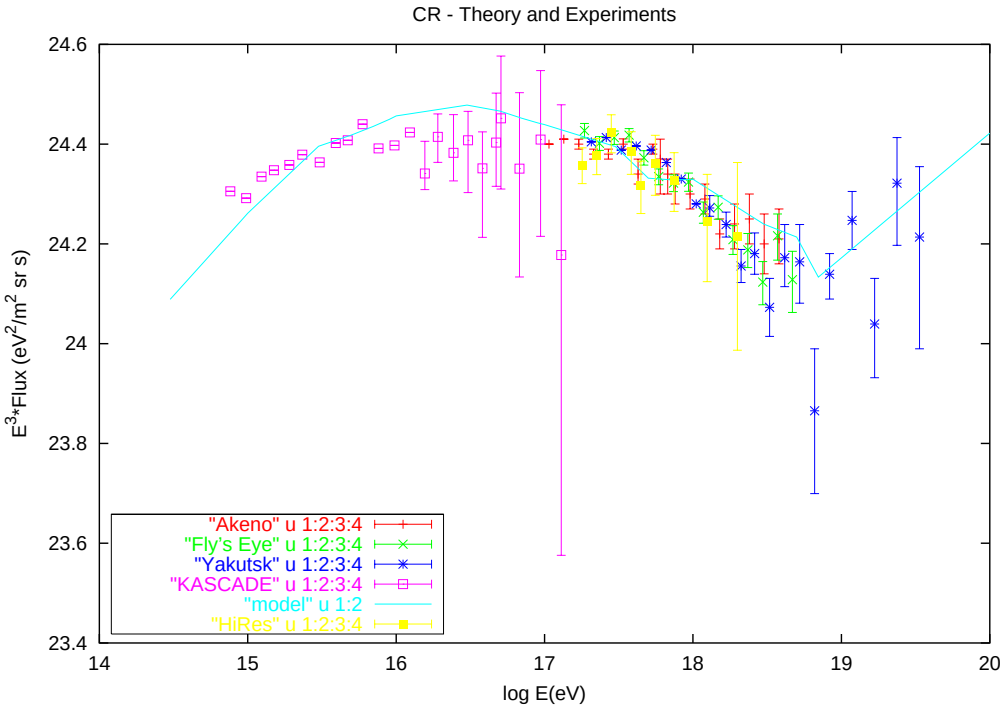

Figure 26: Our fit to the data across PeV through EeV energies. The model can fit the HiRes and other high energy data without any recalibration of the energy scale, while the KASKADE data require a small rescaling by 18 % .

also arise from supernovae, but from those that explode into their own stellar wind, so wind-SN. These supernovae correspond to initial zero age main sequence masses of the predecessor star of about 20 solar masses and more. This theory suggests that the knee can be derived from a careful consideration of the acceleration of particles in a stellar wind, using the Solar wind analog, the Parker spiral for the magnetic field topology in the wind. Different angles with respect to the symmetry axis in the wind correspond to different obliquities of the shock and its acceleration, going from one limit near the pole, to the extreme obliqueness near the equator. We can then account quantitatively for the energy of the knee and the slope beyond the knee, as well as the switch near $3 \cdot 10^{18}$ eV. In the last three years the further development of our theory suggests that antiprotons can all be explained within this picture, in flux and in spectral behavior, as can the gamma ray spectrum of the Galaxy and the positron fraction. The CASA-MIA, MAKET-ANI, KASKADE, AGASA, YAKUTSK and HiRes arrays have provided further tests, and it has been possible to show that the theory can account for all data available now; the knee is properly described, even in its detailed chemical composition, as is the final cutoff and the transition to the new component. Fig. 26 shows the spectral fit to the cosmic ray data across the entire energy range from below PeV, 10^{15} eV, to beyond EeV, 10^{18} eV.

The sharpness of the knee feature near $3 \cdot 10^{15}$ eV, visible considering all data available, which show all particles at once; this appears to be consistent in the various chemical elements as far as can be determined today (strictly a bend in the spectrum at a given rigidity, or energy divided by charge of the fully stripped nucleus), has rather strong consequences for the explosion mechanism of the supernovae in the corresponding mass range. Since the feature in the cosmic ray spectra is required to be the same in all supernovae contributions, our theory shows, that there is a strong correlation between stellar spin, magnetic field and explosive energy - exactly as was proposed by Kardashev in 1964. This means that the core of the

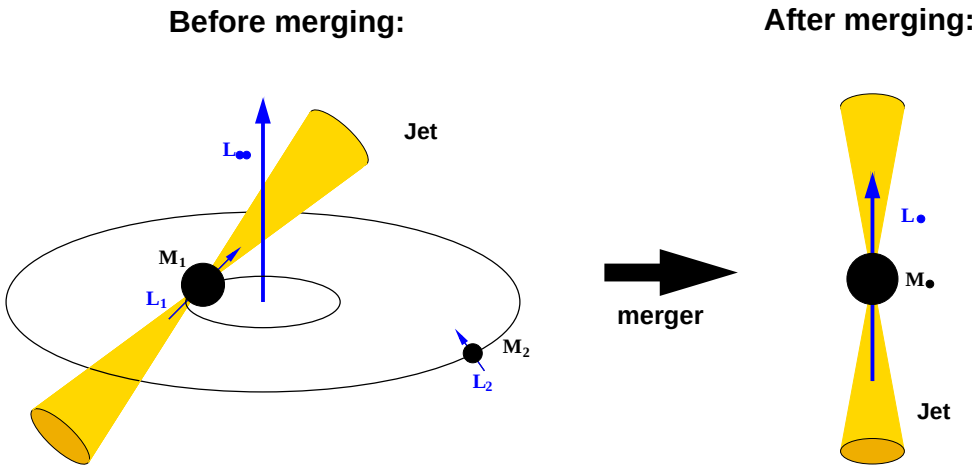

Figure 27: The principle of the spin-flip of the more massive back hole induced by the orbital angular momentum of the secondary black hole.

star collapses, is flattened by the angular momentum barrier into a flat small disk, and stops collapsing at that moment. Then the angular momentum is removed by Alfvén waves, which are torsional, and precisely the potential energy of the small flat disk is transmitted to the envelope which is thus exploded, while the core then collapses and liberates the abundant neutrinos as observed. Putting in numbers then implies several consequences, as we have shown: a) These supernovae all have an energy of explosion near 10^{52} ergs, consistent with the known data (such as SN1998bw). b) These supernova explosions are strongly anisotropic. c) If a way could be found to deduce a correction for the anisotropy, then these supernovae may become a new standard candle in cosmology, much brighter than any other.

5.3 Merging of Black Holes, Spin-Flips of Massive Black Holes, and Gravitational Waves

Today the work by the Hubble Space Telescope has shown convincing evidence that almost all galaxies have a central massive black hole. The mass of this black hole correlates well with the total baryonic mass of the old spheroidal stellar population, and correlates extremely well with the velocity dispersion of the central stellar population. In earlier work we have shown that such correlations can be readily interpreted as the result of the competition of star formation and accretion as a function of radial distance in the disk of a galaxy, when considered as a gigantic accretion disk, and subsequent mergers between galaxies. As soon as two galaxies merge which both have central black holes, the two black holes spiral in towards each other under the rather strong influence of dynamical friction, with time scales of order 10^7 to 10^8 years. This inspiraling slows down considerably when the two black holes get as close as the core radius of the central star distribution, of order a parsec or so. At that point more detailed consideration is required. The central stellar distribution is carved out into a broad belt, whose subpopulation of red and blue giant stars has their winds turned into tails by radiation pressure from the central accretion disk. These winds and their dust may constitute the ubiquituous torus so often inferred from X-ray absorption, from the far-infrared emission, from scattering of emission lines, or from the statistics of visibility of the broad emission lines. In recent work we have expanded this concept to include the final stages of the merger, now between the two central black holes. Fig. 27 shows our basic concept of the spin-flip of two merging black holes.

When the two black holes get sufficiently close to induce gravitational radiation, it becomes necessary to include the spin orientation of the orbit of the two black holes, and their intrinsic spin. Focussing on the more massive black hole, and treating the second black hole in a test particle limit, we have used a post-Newtonian approximation to derive the properties of the gravitational waves, and the reaction of the two orbiting black holes. The interesting question is whether the angular momentum transport by the gravitational wave emission will remove most of the orbital angular momentum of the secondary black hole. This would thus lead to a final merged black hole whose total angular momentum has a direction which is little modified from the pre-merger direction of the spin of the primary black hole. Our calculations have shown that the opposite happens: the removal of orbital angular momentum has been demonstrated to have a very strong dependence on the angle between orbital spin of the secondary black hole and the intrinsic spin of the primary black hole. This dependence is so strong that the final black hole spin after the merger is not only turned around, but also remains high relative to the maximum spin allowed. This shows that a merger of a maximally rotating black hole with a secondary black hole with an orbital spin axis which is in a very different direction can lead to a spin flip, with the new spin again near maximum. A maximal spin both in the pre- and the post-merger state for the dominant black hole may be crucial to understand the hadronic interactions near the base of the jet. The key point is that the orbital angular momentum of the secondary black hole is not completely removed by gravitational waves, as one might have expected. Of all proposed models, this, it turns out, is the best viable explanation for the X-shaped radio galaxies. Our recent calculations show that the spin dependence of the black hole mergers needs to be taken into account because it severely modifies the final gravitational wave emission. This may have consequences for the template used to look for the weak signal from black hole mergers.

People involved: P.L. Biermann, G. Bayer (now Univ. of Ankara), S. Casanova, M. Chirvasa (now MPI Grav. Physics, Potsdam), A. Curutiu, H. Falcke, C. Galea (now Univ. of Nijmegen, Netherlands), L. Haroyan (now Italy), T. Kellmann, H. Lee (also at Chungnam Nat. Univ., Daejeon, Korea), I. Maris, S. Markoff (now at MIT), A. Meli, F. Munyaneza, N. Nemes (now in Japan), O. Nenestyan, G. Pavalas, A. Popescu, R. Roman, P. Simon (now at Univ. of Bonn), O. Tascau, V. Tudose, A. Vasile, F. Yuan (now at Harvard), C. Zier.

Collaborations: E.-J. Ahn (Univ. of Seoul, Korea; Univ. of Chicago), J. Becker (Univ. of Wuppertal), H. Blümer (FZ Karlsruhe), Z. Cao (Univ. of Utah), A. Donea (Univ. of Adelaide, Australia), R. Engel (Bartol Res. Inst., Newark, DE, USA; FZ Karlsruhe), T. Enßlin (MPI Astrophysics, Munich), R. Fender (Univ. of Amsterdam), K.-H. Kampert (Univ. of Karlsruhe), H. Kang (Pusan Nat. Univ., Korea), U. Klein (Univ. of Bonn), T. Kneiske (Univ. of Würzburg), G. Krishna (Nat. Center for Radio Astron., Pune, India), P. Kronberg (Univ. of Toronto, Canada; Los Alamos Nat. Lab., New Mexico, USA), N. Langer (Univ. of Utrecht, Netherlands), K. Mannheim (Univ. Würzburg), G. Medina-Tanco (Univ. of Sao Paolo), S. Moiseenko (Space Research Inst., Moscow), B. Nath (Raman Res. Inst., Bangalore, India), K. Petrovay (Univ. of Budapest), R. Protheroe (Univ. of Adelaide, Australia), G. Pugliese (Univ. of Cal. Santa Cruz, USA), W. Rhode (Univ. of Wuppertal), H. Rottmann (Univ. of Bonn), M. (Univ. of Bucarest, Romania), D. Ryu (Chungnam Nat. Univ., Daejeon, Korea), N. Sanchez (Observ. de Paris), G. Schäfer (Univ. of Jena), E.-S. Seo (Univ. of Maryland, USA), G. Sigl (Inst. for Astrophys., Paris), Ramin Sina (Univ. of Maryland, USA), T. Stanev (Bartol Res. Inst., Newark, DE, USA), S. Ter-Antonyan (Univ. of Erewan, Armenia), H. de Vega (Univ. of Paris), A. Wandel (Hebrew Univ., Jerusalem), Y. Wang (Purple Mountain Obs., Chin. Acad. of Science, Nanjing), S. Westerhoff (Columbia Univ., New York City, USA)